UK Biobank

Brain Imaging Documentation

http://www.ukbiobank.ac.uk

UK Biobank Brain Imaging Documentation

Version 1.9

September 2022

primary documentation authors:

Stephen M. Smith, Fidel Alfaro-Almagro and Karla L. Miller

Wellcome Centre for Integrative Neuroimaging (WIN-FMRIB), Oxford University on behalf of UK Biobank

Contributors to UK Biobank Brain Imaging

Scientific direction: Stephen Smith and Karla Miller (WIN-FMRIB, Oxford), Paul Matthews (Imperial).

Core image processing: Fidel Alfaro-Almagro and Stephen Smith (WIN-FMRIB, Oxford).

Additional input on acquisitions, protocols, reconstruction, image processing, IT/informatics: Jesper Andersson, Stuart Clare, Gwenaëlle Douaud, Eugene Duff, Ludovica Griffanti, Moises Hernandez Fernandez, David Flitney, Saad Jbabdi, Mark Jenkinson, Heidi Johansen-Berg, Paul McCarthy, Duncan Mortimer, Gholamreza Salimi-Khorshidi, Thomas Okell, Stamatios Sotiropoulos, Benjamin Tendler, Emmanuel Vallee, Chaoyue Wang, Matthew Webster (WIN-FMRIB, Oxford), Thomas Nichols, Robert Esnouf, Jon Diprose, Colin Freeman (BDI/BMRC, Oxford), Steve Garratt, Sarah Hudson, Niels Oesingmann (UK Biobank Imaging), Alan Young, John Miller, Jonathan Price (NDPH, Oxford), Peter Weale, Iulius Dragonu (Siemens UK), Neal Bangerter (Brigham Young University, USA), Tony Stoecker (Bonn, Germany), Kamil Ugurbil, Essa Yacoub, Steen Moeller, Eddie Auerbach (CMRR, University of Minnesota, USA), Simon Cox, Andrew McIntosh (Edinburgh University, UK), Alessandro Daducci (EPFL, Switzerland), Matthias Günther (Fraunhofer Mevis, Bremen, Germany), Andreas Bartsch (Heidelberg, Germany), Doug Greve, Bruce Fischl, Jonathan Polimeni (MGH, USA), Anna Murphy (Manchester University, UK), Junqian Gordon Xu (Mount Sinai Medical Center, USA), Michael Chappell, Martin Craig (Nottingham University, UK), Takuya Hayashi (Riken, Kobe, Japan), David Thomas, Daniel Alexander, Gary Zhang, Enrico Kaden (UCL, UK), Chris Rorden (University of South Carolina, USA), Fred Barkhof (VU Amsterdam, Netherlands), Deanna Barch, Greg Burgess, Nick Bloom, Dan Nolan, Michael Harms, Matt Glasser (Washington University St. Louis, USA), Christian Beckmann (Donders Nijmegen, Netherlands).

Image processing funding: FAA is supported by UK Biobank. SMS, KLM and compute costs are supported by Wellcome Trust (203139/Z/16/Z, 202788/Z/16/Z, 098369/Z/12/Z, 215573/Z/19/Z). The core image processing is carried out on the clusters at the Oxford Biomedical Research Computing (BMRC) facility and WIN-FMRIB (part of the Wellcome Centre for Integrative Neuroimaging). BMRC is a joint development between the Wellcome Centre for Human Genetics and the Big Data Institute, supported by Health Data Research UK and the NIHR Oxford Biomedical Research Centre.

We are also extremely grateful to all UK Biobank study participants.

Contents

1 Introduction

This documentation describes the brain imaging component of the UK Biobank prospective epidemiological study. It provides details of the acquisition protocols, image processing pipeline, image data files and derived measures (IDPs - imaging-derived phenotypes) of brain structure and function.

Researchers wanting to avoid reading the full technical detail relating to the imaging and image processing may wish to concentrate on Sections 1 and 4.

1.1 UK Biobank - background

UK Biobank is a prospective cohort study of over 500,000 individuals from across the United Kingdom. Participants, aged between 40 and 69, were invited to one of 22 centres across the UK between 2006 and 2010. Blood, urine and saliva samples were collected, physical measurements were taken, and each individual answered an extensive questionnaire focused on questions of health and lifestyle. The resource will provide a picture of how the health of the UK population develops over many years and it will enable researchers to improve the diagnosis and treatment of common diseases.

UK Biobank has collected genetic data on every participant. It has also begun to invite back some of the original participants for brain, heart and body imaging. It is the brain imaging that is the subject of this document.

The UK Biobank resource is open to the research community and it will grow and develop over time. It is a UK Biobank data access policy that findings that use UK Biobank data should be fed back to UK Biobank and made available to other researchers. Researchers associated with UK Biobank (such as those helping run the brain imaging) do not get preferential data access and are not able to carry out their own research with data until it is made available for all researchers.

1.2 Referencing use of Brain Imaging Data

The primary citations for UK Biobank brain imaging are listed below. If you make use of pre-processed image data or the IDPs (summary measures described below and available from UK Biobank), we would be grateful if this can be made clear in publications; this will help with ongoing justification to funders for this component of UK Biobank. Appropriate example text might begin with the following, with additional specific details potentially extracted from this document and the papers referenced below: "***Our study made use of [imaging-derived phenotypes / pre-processed image data] generated by an image-processing pipeline developed and run on behalf of UK Biobank (Alfaro-Almagro, NeuroImage 2018)***". Of course, as is always the case, UK Biobank Data Access does not require you to add (individual or groupwise) additional co-authorships.

- *Online brain imaging documentation - this document:*
  UK Biobank Brain Imaging Documentation.
  Stephen Smith, Fidel Alfaro Almagro and Karla Miller.
  biobank.ctsu.ox.ac.uk/crystal/crystal/docs/brain_mri.pdf

- *Primary citation for brain imaging in UK Biobank:*
  Multimodal population brain imaging in the UK Biobank prospective epidemiological study.
  K.L. Miller, F. Alfaro-Almagro, N.K. Bangerter, D.L. Thomas, E. Yacoub, J. Xu, A.J. Bartsch, S. Jbabdi, S.N. Sotiropoulos, J.L.R. Andersson, L. Griffanti, G. Douaud, T.W. Okell, P. Weale, I. Dragonu, S. Garratt, S. Hudson, R. Collins, M. Jenkinson, P.M. Matthews, and S.M. Smith.
  Nature Neuroscience, 19(11):1523–1536, 2016.

- *Primary citation for the brain imaging processing pipeline and IDPs:*
  Image processing and Quality Control for the first 10,000 brain imaging datasets from UK Biobank.
  F. Alfaro-Almagro, M. Jenkinson, N.K. Bangerter, J.L.R. Andersson, L. Griffanti, G. Douaud, S.N. Sotiropoulos, S. Jbabdi, M. Hernandez-Fernandez, E. Valee, D. Vidaurre, M. Webster, P. McCarthy, C. Rorden, A. Daducci, D.C. Alexander, H.

Zhang, I. Dragonu, P.M. Matthews, K.L. Miller and S.M. Smith.
NeuroImage 166(400–424), 2018.

- *Primary citation for confound modelling for UKB brain imaging:*
  Confound modelling in UK Biobank brain imaging.
  F. Alfaro-Almagro, P. McCarthy, S. Afyouni, J.L.R. Andersson, M. Bastiani, K.L. Miller, T.E. Nichols, S.M. Smith.
  NeuroImage 224(117002), 2021.

1.3 UK Biobank Brain Imaging

Because of the very large numbers of study participants, the entire brain imaging protocol has to be completed within 35 minutes. Much effort has been made to optimise image quality given this strict limitation, and to achieve a suitable balance (of time/quality/robustness) between the different modalities acquired. The brain imaging data acquisition primarily includes 6 modalities, covering structural, diffusion and functional imaging, with the order below reflecting the actual acquisition ordering in the majority of subjects (the earliest subject had slightly different modality ordering):

- **T1** A T1-weighted structural image. T1-weighted imaging is a structural technique with high-resolution depiction of brain anatomy, having strong contrast between grey and white matter, reflecting differences in the interaction of water with surrounding tissues (tissue T1 relaxation times). This modality provides IDPs primarily relating to volumes of brain tissues and structures. It is also critical for calculations of cross-subject and cross-modality alignments, needed in order to process all other brain modalities.
- **rfMRI** Resting-state functional MRI timeseries data. Resting-state functional MRI measures changes in blood oxygenation associated with intrinsic brain activity (i.e., in the absence of an explicit task or sensory stimulus). Derived IDPs estimate the apparent connectivity between pairs of brain regions, as reflected in the presence of spontaneous co-fluctuations in signal (i.e., the appearance of a connection based on co-activity, as opposed to a structural tract from dMRI). Other IDPs reflect the amplitude of spontaneous fluctuation within each region.
- **T2_FLAIR** A T2-weighted FLAIR structural image. T2-weighted imaging is a structural technique with contrast dominated by signal decay from interactions between water molecules (T2 relaxation times). Image intensity is primarily related to pathology, with relatively subtle signal differences between grey and white matter. T2 images depict alterations to tissue compartments typically associated with pathology (e.g., white matter lesions).
- **dMRI** Diffusion MRI. Diffusion-weighted imaging is a structural technique that measures the ability of water molecules to move within their local tissue environment. Water diffusion is measured along a range of orientations, providing two types of IDPs. Local (voxel-wise) estimates of diffusion properties reflect the integrity of microstructural tissue compartments (e.g., diffusion tensor estimates). Long-range estimates based on tract-tracing (tractography) reflect structural connectivity between pairs of brain regions.
- **SWI** Susceptibility-weighted imaging. Susceptibility-weighted imaging is a structural technique that is sensitive to magnetized tissue constituents (magnetic susceptibility). Data from one scan (including phase and magnitude images from two echo times) can be processed in multiple ways to reflect venous vasculature, microbleeds or aspects of microstructure (e.g., iron, calcium and myelin).
- **tfMRI** Task functional MRI timeseries data. Task functional MRI uses the same measurement technique as resting-state fMRI, while the subject performs a particular task or experiences a sensory stimulus. Derived IDPs relate to the strength of response to the specific task (or a specific component of a more complex cognitive process) within a given anatomical brain region. The task used in Biobank was chosen to engage a range of high-level cognitive systems.

In 2020 the COVID-19 pandemic caused a pause in UKB imaging. In February 2021, imaging was re-started with the specific goal of bringing back approximately 1000 previously-scanned participants who had later become infected with SARS-CoV-2, along with a well-matched control group. The imaging protocol was unchanged apart from the addition of ASL. Once general second-scan imaging resumes, ASL will continue to be included.

- **ASL** Arterial spin labelling. Arterial spin labelling is a physiological imaging technique that uses blood water as an endogenous tracer to measure perfusion of the brain tissue. Two types of IDPs are derived from this data that reflect the physiological state of the tissue and the blood vessels supplying it: cerebral blood flow (CBF) IDPs reflect the amount of blood perfusing different brain regions, and arterial transit time (ATT) IDPs relate to how long it takes blood to travel from the neck to a given region of interest.

In addition to releasing raw data, an image processing pipeline has been run that has generated processed versions of the data, using publicly available image processing tools, primarily taken from FSL (the FMRIB Software Library [Jenkinson et al., 2012], version 5.0.10) and more recently also FreeSurfer [Dale et al., 1999] version 6.0 (version=6-20170118 build-stamp=v6.0.0-2beb96c). For example, the T1 structural image has been processed to remove non-brain parts of the image, and to segment the brain image into different tissue types. The pipeline has also been used to generate several QC (quality control) measures.

For all brain imaging modalities, the pipeline has also been used to generate many IDPs (image-derived phenotypes). These numerical pipeline outputs aim to be objective quantifications of different aspects of brain structure and function. IDPs range from simple gross measures, such as total brain volume, to very specific detailed measures, such as average functional connectivity between two specific brain regions. The goal is for IDPs to be useful summary measures derived from the imaging data, that can be used in analyses to relate to other non-imaging variables in UK Biobank, such as health outcome measures. Each IDP is presented as a separate data field within the UK Biobank showcase http://www.ukbiobank.ac.uk/data-showcase.

Over the coming months/years, the goal is to expand the analysis pipeline, including state of the art processing from a broader range of methods/models and software toolkits, where this will increase the quality, robustness and scope of processing applied and IDPs generated. One high priority is to adapt the FreeSurfer / Human Connectome Project pipelines to achieve cortical surface modelling (FreeSurfer cortical structural modelling has now been incorporated and released; HCP-style cortical modelling of fMRI data will hopefully be available in late 2022).

Some image data quality control (a combination of manual and automated checking) has taken place as part of the data processing; for example, IDPs are not generated for datasets that have been identified as being incomplete or very badly affected by artefacts. However, UK Biobank is committed to making available to researchers all imaging data acquired (see below for more details), and not just imaging datasets judged to be of very high quality. This is in part because different researchers may have different definitions of "acceptable quality", and also because some researchers may want to develop their own processing pipelines to detect/correct image data quality problems. Therefore for any research carried out on the basis of the image data and IDPs, it is important to verify the quality of the datasets used in that research.

An email discussion list has been setup for researchers wanting to discuss any aspects of the UK Biobank brain imaging protocols, data and analysis: https://www.jiscmail.ac.uk/cgi-bin/webadmin?A0=UKB-NEUROIMAGING

1.4 What's new in documentation / data-release versions

- **v1.9 September 2022.** (Including an interim data release of initial COVID-study data in 2021.) Added 4k new subjects, plus 2k second-scan subjects (including 1k COVID+ participants and 1k controls). First release that includes ASL data and QSM modelling. 47k subjects total and 5k second-scans total.
- **v1.8 December 2020.** Added 3k new subjects, plus 1.4k second-scan subjects. 43k subjects total and 3k second-scans total.
- **v1.7 January 2020.** Added 18k new subjects, plus 1.5k second-scan subjects. Added new confound variables. 40k subjects total.
- **v1.6 May 2019.** Added FreeSurfer processing and IDPs. 22k subjects.
- **v1.5 August 2018.** General documentation update, including new information about imaging confounds. 22k subjects.
- **v1.4 December 2017.** Minor documentation update. 15k subjects.
- **v1.3 January 2017.** Added white matter lesion segmentation and associated IDP. Added cortical ROIs' grey matter volume IDPs. 10k subjects.

- **v1.2 August 2016.** Added resting-state fMRI fluctuation amplitude IDPs. 5k subjects.
- **v1.1 January 2016.** Minor documentation changes. 5k subjects.
- **v1.0 October 2015.** Original data release and documentation. 5k subjects.

2 Image acquisition protocols

This section describes the imaging hardware and acquisition protocols (in the order that the different modalities are acquired within the imaging session). The full protocol PDF (as auto-generated by the scanner) is provided at http://biobank.ctsu.ox.ac.uk/crystal/refer.cgi?id=2367; the most important protocol parameters are given below. Additional protocol details (including the "EDX" Siemens protocol file, diffusion directions file, fMRI slice timing information, etc.) are provided at the https://www.fmrib.ox.ac.uk/ukbiobank/protocol/ website.

2.1 Brain imaging hardware

The scanner is a standard Siemens Skyra 3T running VD13A SP4 (as of October 2015), with a standard Siemens 32-channel RF receive head coil.

Initial data was from a single scanner dedicated to UK Biobank imaging, in Cheadle Manchester. In 2017 two further identical centres (in Newcastle and Reading) began scanning.

2.2 Echo-planar imaging

The EPI-based acquisitions (dMRI, rfMRI and tfMRI) utilize simultaneous multi-slice (multiband) acceleration [Larkman et al., 2001, Moeller et al., 2010]. Biobank uses pulse sequences and reconstruction code from the Center for Magnetic Resonance Research (CMRR), University of Minnesota https://www.cmrr.umn.edu/multiband. These developments were partially generated as part of the Human Connectome Project (HCP, NIH grant 1U54MH091657), as described in [Ugurbil et al., 2013].

The fMRI data and primary dMRI data are all acquired with AP (anterior-posterior) phase encoding direction.

Distortion correction of EPI requires an estimate of the static field map. This fieldmap is derived from pairs of spin-echo EPI acquisitions with opposite phase encoding directions, acquired as part of the dMRI dataset; in addition to the primary dMRI data, 3 b=0 images are acquired with reversed phase encoding for later fieldmap estimation (along with 3 b=0 images with standard phase encoding). The estimated fieldmap is used for distortion correction in both the dMRI and fMRI datasets. This aproach was found to have similar accuracy to separate fieldmap acquisitions in much shorter time and with greater robustness against head motion.

2.3 Setup, shimming

Duration: 2 minutes

It is critical to achieve maximally consistent spatial coverage of scans in the presence of differences in subject positioning and head size. For each scan, the field-of-view is automatically determined based on Siemens' auto-align software, which aligns a scout scan to an atlas. In the infrequent situation where auto-align failed, alignment was set by the radiographer.

T1 and T2 structurals are acquired using straight sagittal orientation (i.e., with the field-of-view aligned to the scanner axes). fMRI (task and resting-state), dMRI and SWI utilise slice angling to minimise the superior-inferior field-of-view, thus optimising volume acquisition speed. Using the population brain size and shape results from [Mennes et al., 2014], imaging matrix is angled such that the front of the brain is tilted down (relative to the imaging matrix) by 16°, with respect to the AC-PC line.

Shim field accuracy is critical for data quality, and was found to be suboptimal when using default settings on the MRI scanner, particularly for the simultaneous multi-slice EPI acquisitions. Initially, shim quality was improved by manually iterating the shimming process 3 times; this process which was later replaced by a single shim using a reduced shimming field-of-view, thereby improving resolution of the acquired field map. The scans are prescribed to avoid any subsequent re-shimming during the entire protocol.

2.4 T1-weighted structural imaging

Resolution: 1x1x1 mm
Field-of-view: 208x256x256 matrix
Duration: 5 minutes
3D MPRAGE, sagittal, in-plane acceleration iPAT=2, prescan-normalise

The superior-inferior field-of-view is large (256mm), at little cost, in order to include reasonable amounts of neck/mouth, as those areas will be of interest to some researchers.

2.5 Resting-state functional MRI

Resolution: 2.4x2.4x2.4 mm
Field-of-view: 88x88x64 matrix
Duration: 6 minutes (490 timepoints)
TR: 0.735 s
TE: 39ms
GE-EPI with x8 multislice acceleration, no iPAT, flip angle 52°, fat saturation

As implemented in the CMRR multiband acquisition, a separate "single-band reference scan" is also acquired. This has the same geometry (including EPI distortion) as the timeseries data, but has higher between-tissue contrast to noise, and is used as the reference scan in head motion correction and alignment to other modalities.

2.6 T2-weighted FLAIR structural imaging

Resolution: 1.05x1x1 mm
Field-of-view: 192x256x256 matrix
Duration: 6 minutes
3D SPACE, sagittal, in-plane acceleration iPAT=2, partial Fourier = 7/8, fat saturation, elliptical k-space scanning, prescan-normalise

After early piloting, a standard T2/PD-weighted acquisition was dropped due to a combination of factors such as overall value and timing practicalities. However a T2-weighted FLAIR image is acquired, which is generally of good quality and which shows strong contrast for white matter hyperintensities.

2.7 Diffusion imaging

Resolution: 2x2x2 mm
Field-of-view: 104x104x72 matrix
Duration: 7 minutes (including 36 seconds phase-encoding reversed data)
5x b=0 (+3x b=0 blip-reversed), 50x b=1000 s/mm^2, 50x b=2000 s/mm^2
Gradient timings: δ=21.4 ms, Δ=45.5 ms; Spoiler b-value = 3.3 s/mm^2
SE-EPI with x3 multislice acceleration, no iPAT, fat saturation

For the two diffusion-weighted shells, 50 distinct diffusion-encoding directions were acquired (and all 100 directions are distinct). The diffusion prepraration is a standard ("monopolar") Stejskal-Tanner pulse sequence. This enables higher SNR due to a shorter echo time (TE=92ms) than than a twice-refocused ("bipolar") sequence. This improvement comes at the expense of stronger eddy current distortions, which are removed in the image processing pipeline.

2.8 Susceptibility-weighted structural imaging

Resolution: 0.8x0.8x3 mm
Field-of-view: 256x288x48 matrix
Duration: 2.5 minutes
Two echos, TE=9.42,20 ms
3D, axial, in-plane acceleration iPAT=2, partial Fourier = 7/8, prescan-normalise

To date the magnitude and phase images have been saved for each RF coil and echo time separately.

2.9 Task functional MRI

As for rfMRI, except:
Duration: 4 minutes (332 timepoints)

The task is the Hariri faces/shapes "emotion" task [Hariri et al., 2002, Barch et al., 2013], as implemented in the HCP, but with shorter overall duration and hence fewer total stimulus block repeats. The participants are presented with blocks of trials and asked to decide either which of two faces presented on the bottom of the screen match the face at the top of the screen, or which of two shapes presented at the bottom of the screen match the shape at the top of the screen. The faces have either angry or fearful expressions.

The ePrime script that controls the video presented to the participant is derived from the one used by the HCP, and is available at http://biobank.ctsu.ox.ac.uk/crystal/refer.cgi?id=1462.

2.10 Arterial Spin Labelling

Resolution: 3.4x3.4x4.5 mm (T2-blurring reduces the effective resolution in the slice direction)
Field-of-view: 64x48x32 matrix
Duration: 2 minutes
Preparation: Multi-postlabelling delay pseudocontinuous arterial spin labelling, labelling duration 1800 ms, postlabelling delays 400, 800, 1200, 1600 and 2000 ms, labelling plane offset from the centre of the imaging volume 90 mm
Readout: 2-shot segmented 3D-GRASE, left-right phase encoding, refocussing flip angle 120°
Background suppression: pre-saturation and two inversion pulses (timed to perfectly null tissues with T1 = 700 ms and 1400 ms, 100 ms prior to excitation)
Volumes: one label/control pair per postlabelling delay plus one calibration (M0) volume without labelling or background suppression (effective TR 5000 ms).

This pulse sequence is part of the fme_ASL_collection and was kindly provided by Matthias Günther and colleagues at Fraunhofer Mevis, Bremen, Germany. It is comparable to the multi-postlabelling delay sequence described in [von Samson-Himmelstjerna et al., 2016]. Multiple postlabelling delays were used to allow the fitting of both perfusion (CBF) and transit time (ATT) and improve robustness to delayed blood arrival. The labelling plane is fixed parallel to the imaging slices, so the image orientation was angled closer to true axial than the other modalities to avoid the labelling plane coinciding with the brain-feeding arteries too far from scanner isocentre. The main background suppressed ASL scans are scaled up by a factor of 10 relative to the calibration (M0) volume to improve the dynamic range of the ASL signal.

2.11 Compatibility across different phases of imaging

Ideally the imaging protocol will stay fixed over time. However, early improvements in the dMRI and T2_FLAIR protocols were found to be very valuable, resulting in significant enough data improvements to outweigh the priority of holding things perfectly constant (and taking into account the relatively small numbers of datasets affected). This change was made at the start of protocol

"Phase 3"; the different phases are described in detail below. A variable available in the UK Biobank database (*Acquisition protocol phase*) specifies which protocol phase (currently from 1 to 5) was used for a given subject.

2.11.1 Protocol Phase 1

Only 11 datasets were acquired within this initial phase, after which several major improvements were made in the protocol. None of these datasets were processed with the image processing pipeline to generate IDPs or processed imaging data.

2.11.2 Protocol Phase 2 (compared with Phase 3 and later)

Approximately 500 datasets were acquired with a protocol which, for dMRI and T2_FLAIR, are incompatible with later phases (i.e., are different from what is shown in the Siemens protocol PDF linked above). These differences are now described.

The Phase 2 T2_FLAIR scans did not use elliptical k-space coverage (which was used in later scans to reduce acquisition time with no significant loss in image quality), and used 6/8 partial-Fourier (instead of the later 7/8 partial-Fourier, a change which reduced image blurring in later scans with a small time penalty).

The Phase 2 dMRI scans used "bipolar" (twice-refocused spin echo) diffusion encoding, instead of the "monopolar" (Stejskal-Tanner single spin echo) approach used later. Recent advances in post-processing are able to remove the greater image distortions incurred by monopolar encoding, allowing a reduction in echo time from 112ms to 92ms, providing a substantial increase in SNR and reducing the TR from 4.06s to 3.6s, providing a large reduction in scan time. Other (more minor) differences in Phase 2 dMRI scans (compared with Phase 3) are: one fewer diffusion encoding direction per shell, a larger flip angle (93/180 instead of the later 78/160) and a greater number of blip-reversed b=0 images (5 instead of the later 3).

As described in more detail below, for these early "incompatible" scans, the raw T2_FLAIR and dMRI NIFTI images are available via the UK Biobank database, but have not been used in the full image processing pipeline, and do not have IDPs computed (as these would likely be incompatible with those generated later).

One final minor difference in the Phase 2 scans, which does not present incompatibility problems, is that the rfMRI and tfMRI protocols had additional timepoints (approximately 30s) compared with later scans.

2.11.3 Protocol Phase 4 (compared with Phase 3)

No significant changes were made between Phase 3 and 4. Three superfluous b=0 scans were removed. The T2_FLAIR was moved within the protocol to run after the fMRI scans. A new auto-shimming approach was put in place, with a reduced shimming field-of-view and fewer shim iterations; this saved time and was evaluated to result in very similar shimming quality. A small cross-hair was added to the video display, for subjects to focus on (except during tfMRI).

2.11.4 Protocol Phase 5

No significant changes; CMRR multiband software was upgraded to v12 (R012b).

2.11.5 Protocol Phase 6

No significant changes; CMRR multiband software was upgraded to R014.

2.11.6 Protocol Phase 7

No significant changes; CMRR multiband software was upgraded to R015.

2.11.7 Protocol Phase 8

No significant changes; Siemens scanner software was upgraded with service-pack SP7.

3 Image processing pipeline

The full set of image analysis pipeline scripts are available from `https://www.fmrib.ox.ac.uk/ukbiobank/` - at present the scripts primarily call tools from FSL and FreeSurfer.

3.1 Reconstruction of real-space data from k-space complex data

Images in the "real space" domain were reconstructed from the complex k-space domain in which data are collected. Unless otherwise specified, all images are signal magnitude.

Standard Siemens on-scanner conversion of complex multi-coil data was carried out for the T1 and T2_FLAIR data.

Image reconstruction for the simultaneous multi-slice EPI data (dMRI, rfMRI, tfMRI) was carried out using reconstruction software supplied by CMRR (available from the CMRR web site listed above).

SWI data has, to date, been saved as coil-separated real-space complex data, as it has not yet been possible to carry out appropriate multi-coil combination on the scanner for accurate reconstruction of phase images. This is expected to change in the near future.

3.2 Raw DICOM data conversion to NIFTI and download options

All real-space DICOM image files are converted to NIFTI format using Chris Rorden's conversion tool dcm2niix `https://github.com/rordenlab/dcm2niix`. This tool also generates the diffusion-encoding b values and vectors files.

Image data is available from UK Biobank in both DICOM and (separately) NIFTI formats. Both forms include the raw (non-processed) data, the only differences being that the NIFTI-version T1/T2 structural images are defaced for subject anonymity (as described below), and the full multi-coil (pre-combination) SWI data is only available in the DICOM downloads. An individual zipfile download is for one modality from one subject for one data format (DICOM or NIFTI).

The NIFTI versions are the recommended option, partly because for each modality a small number of simply and consistently named images are provided (e.g., `T1`, `rfMRI`), as opposed to thousands of separate DICOM files (with complex naming conventions). Also, the NIFTI downloads, while overall only being 40% larger than pure-raw DICOM downloads, include not just the the raw images, but also images output by the processing pipeline, for example after gradient distortion correction (for all modalities), and correction for eddy currents and head motion (dMRI data), and artefact removal (rfMRI data).

3.3 Image anonymisation and raw DICOM data access

In order to protect study participant anonymity, the high resolution structural images (T1 and T2) are "defaced". This involves setting voxels in the general regions of the face and ears to zero. This is achieved by estimating a linear transformation between the original data and a standard co-ordinate system (an expanded MNI152 template space), and back-projecting standard-space regions-of-interest into the native data, to allow for masking-out of the face/ears. Testing for overlap between (non-defaced) brain masks and the defacing masks shows only 8 subjects with any overlap at all, and all qualitatively show virtually no loss of brain voxels.

Hence in the NIFTI-format data released by UK Biobank, for the T1 and T2 data, only defaced versions are available (to protect anonymity of study participants). This matches common practice such as that in the HCP. The raw, non-defaced DICOM T1 and T2 data is classified as sensitive by UK Biobank; researchers requiring raw DICOM non-defaced T1/T2 data should contact UK Biobank to discuss this further.

3.4 Data/Folder file organisation and primary T1 QC

For each subject, the raw and processed imaging data files are organised into subfolders according to the different modalities (and described in more detail for each modality below).

When raw data is corrupted, incomplete, missing or otherwise clearly unusable, it is moved into a subfolder (inside the given modality's folder) named `unusable`, and not processed any further (apart from defacing applied to the raw T1 and T2_FLAIR). This "unusable" data is included in the Biobank database, because some researchers may be interested in working with this data, for example, to develop new methods for detecting or even possibly correcting such data.

Next, the evaluation of the T1 data for "usability" then includes a semi-automated QC review of all T1s; here, a trained automated classifier scores all datasets for quality, and any T1 that is close to the "bad data" threshold is carefully manually reviewed [Alfaro-Almagro et al., 2018]. Next, all datasets flagged for making unusable have a final quick (not comprehensive) manual review. Where a T1 is considered to have a serious problem it has been moved into the "unusable" subfolder as described above. This is for datasets where the issue is considered serious enough that the pipeline is unlikely to run well - which could be imaging artefacts/problems or very gross pathologies. More subtle pathologies that are subtle enough that we expect the pipeline to run OK are not treated as "unusable" in this way.

In the case of unusable T1 data, all other modalities' raw imaging data are also considered unusable (because the pipeline cannot function without a usable T1). However, as with the T1 data, all such raw data is still available for download in the NIFTI packages (but without the pipeline processing applied).

In the case of the incompatible (Phase 2) dMRI and T2_FLAIR data (see above for protocol incompatibilities), these also are not processed with the image processing pipeline, but the raw data are moved to an `incompatible` folder, and available for download. For example, some researchers may wish to investigate the possibility of developing analyses which can handle the protocol incompatibilities.

3.5 Gradient distortion correction

Full 3D gradient distortion correction (GDC) is not available on the scanner for EPI data, and so all GDC is applied within the image analysis pipelines. Tools developed by the FreeSurfer and HCP teams are used for applying the correction, available at `https://github.com/Washington-University/Pipelines`. To run these tools also requires a proprietary data file from Siemens which describes the gradient nonlinearities (`coeff.grad`).

3.6 T1 processing

The raw original (defaced) T1-weighted structural image and other T1-derived pipeline outputs are in the folder `T1`.

The full FoV (field-of-view) raw T1 image, after defacing, is `T1_orig_defaced`. Apart from the defacing (and the fact that bias field has already been reduced via the on-scanner "pre-scan normalise" option), this is the raw T1 structural data, without any further processing such as gradient distortion correction.

The FoV is then cut down to reduce the amount of non-brain tissue (primarily blank space above the head and tissues below the brain), and GDC applied. Tools utilised to achieve this robustly include BET (Brain Extraction Tool [Smith, 2002]) and FLIRT (FMRIB's Linear Image Regsitration Tool [Jenkinson and Smith, 2001, Jenkinson et al., 2002]), in conjunction with the MNI152 "nonlinear 6th generation" standard-space T1 template `http://www.bic.mni.mcgill.ca/ServicesAtlases/ICBM152NLin6`. This results in the reduced-FoV T1 head image `T1`.

The data is now nonlinearly warped to MNI152 space using FNIRT (FMRIB's Nonlinear Image Registration Tool [Andersson et al., 2007b, Andersson et al., 2007a]), resulting in the warp transform file `transforms/T1_to_MNI_warp_coef`. A standard-space brain mask is then back-transformed into the space of the T1 (generating `T1_brain_mask`), and applied to the T1 image to generate a brain-extracted T1, `T1_brain`.

Next, tissue-type segmentation is applied using FAST (FMRIB's Automated Segmentation Tool [Zhang et al., 2001]), with outputs in subfolder T1_fast. This provides a hard segmentation into CSF (cerebrospinal fluid), grey matter and white matter (T1_brain_seg), as well as partial-volume images for each tissue type (T1_brain_pve_0, T1_brain_pve_1 and T1_brain_pve_2, respectively). This processing is also used to generate a fully bias-field-corrected version of the brain-extracted T1: T1_unbiased_brain.

These data are then used to carry out a SIENAX-style analysis (Structural Image Evaluation, using Normalisation, of Atrophy: Cross-sectional [Smith et al., 2002]). The external surface of the skull is estimated from the T1, and used to normalise brain tissue volumes for head size (compared with the MNI152 template). Volumes of different tissue types and total brain volume, both normalised for head size, and not normalised, are generated as IDPs and accessible from the UK Biobank database.

The FAST grey matter segmentation is also used to generate a further 139 IDPs, by summing the grey matter partial volume estimates within 139 ROIs. These ROIs are defined in MNI152 space, combining parcellations from several atlases: the Harvard-Oxford cortical and subcortical atlases https://fsl.fmrib.ox.ac.uk/fsl/fslwiki/Atlases and the Diedrichsen cerebellar atlas http://www.diedrichsenlab.org/imaging/propatlas.htm . The previously estimated warp field (taking the subject's data into standard space) is inverted and applied to the ROIs, to generate a version of the ROIs in native space, for masking onto the segmentation.

Subcortical structures (shapes and volumes) are modelled using FIRST (FMRIB's Integrated Registration and Segmentation Tool [Patenaude et al., 2011]). The shape and volume outputs for 15 subcortical structures (in files *.bvars and *.vtk - see http://fsl.fmrib.ox.ac.uk/fsl/fslwiki/FIRST/UserGuide) are stored in the T1_first subfolder. A single summary image, with a distinct integer value coding for each structure, is T1_first_all_fast_firstseg. The volumes of the different structures are saved as IDPs in the Biobank database.

The T1 images are also processed with FreeSurfer. Where available, the T2_FLAIR is used in conjunction with the T1 to achieve more accurate cortical modelling than possible with the T1 only. For some derived measures, such as cortical thickness, there is a clear bias in thickness estimated when using both inputs vs. just the T1, and so we would recommend either using just measures derived from analyses using both inputs, or attempting deconfounding. The variable indicating this information is at http://biobank.ndph.ox.ac.uk/showcase/field.cgi?id=26500 in the UK Biobank database. FreeSurfer outputs (images, surface files and summary outputs) are available for download in a single zipfile per subject. These live in the FreeSurfer subfolder.

The primary FreeSurfer modelling is of the cortical surface [Dale et al., 1999, Fischl et al., 1999a, Fischl et al., 1999b]. Surface atlases are used to extract IDPs relating to standard atlas regions' surface area, volume and mean cortical thickness [Fischl et al., 2004, Desikan et al., 2006]. Subcortical regions are extracted using FreeSurfer's aseg tool [Fischl et al., 2002], and also further sub-segmentation of some subcortical regions is carried out [Iglesias et al., 2015], resulting in additional IDPs. Additional "grey-white contrast" cortical region IDPs are created, expressed as the fractional contrast between white and grey intensities (as sampled either side of the grey-white cortical boundary): (W-G)/((W+G)/2).

The FreeSurfer outputs are then QC checked. We use the Qoala-T approach [Klapwijk et al., 2019] to check FreeSurfer outputs, supplemented by manual checking of all outputs close to threshold[1]. Any FreeSurfer outputs failing this QC are not included in the FS zipfile downloads or FreeSurfer IDPs.

3.7 T2_FLAIR processing

The original (defaced) T2-weighted structural image and other pipeline outputs are in folder T2_FLAIR.

The full FoV T2 image, after defacing, is T2_FLAIR_orig_defaced.

The T2 image is linearly aligned to the T1 using FLIRT, and the resulting transform is then combined with various transforms derived from the T1, in order to transform the T2 directly from the original space into both the individual subject's T1 space and MNI standard space. By analogy with the T1-related images described above, this results in images T2_FLAIR and T2_FLAIR_brain, and a bias-corrected version of the latter T2_FLAIR_brain_unbiased (these being in the space of the T1), as

[1]Training data for running Qoala-T was kindly supplied by Simon R Cox, Xueyi Shen, Lianne M Reus, Clara Alloza, Mathew A Harris, Helen L. Alderson, Stuart Hunter, and Emma Neilson

well as T2_FLAIR_brain_to_MNI (MNI-space version).

The total volume of white-matter hyperintensities (WMHs, or white matter lesions) is estimated to generate an additional IDP. This is primarily utilising the T2_FLAIR data, but also the T1 data; this lesion segmentation is automatically carried out using the BIANCA tool[Griffanti et al., 2016].

3.8 SWI processing

The original SWI data and other pipeline outputs are in folder SWI. This data can provide a range of maps with distinct features related to magnetic susceptibility. Phase images can be used for quantitative susceptibility mapping, magnitude data can be used to calculate T2* relaxation rates, and both magnitude and phase are used for generating venograms (see below) and for visualizing hemosiderin in microbleeds.

Combining phase images across coils requires care due to anomolous phase transitions in regions of focal signal dropout for a given coil. Currently, all coil channels are saved separately to enable combination of phase images in post-processing. Each coil channel phase image is first high-pass filtered to remove low-frequency phase variations (including both coil phase profiles and field distortion from bulk shape). A combined complex image is generated as the sum of the complex data from each coil (unfiltered magnitude and filtered phase), and the final phase image (filtered_phase) is the phase of this summation. Careful inspection of a small number of subjects found no anomolous phase transitions from individual channels in the final combined image.

Venograms (SWI) were calculated using an established reconstruction [Haacke et al., 2004], in which magnitude images are multiplied by a further filtration of the phase data to enhance the appearance of veins. The phase image is first thresholded (such that only paramagnetic susceptibility is non-unitary) and then taken to the fourth power to enhance contrast in veins. The chosen power represents a tradeoff between venous-tissue contrast and noise in the phase data.

R2* values were calculated from the magnitude data. First, a single magnitude image is calculated for each of the two echo times TE1 and TE2. This is calculated by taking the square of the magnitude image from each individual coil channel, summing across channels, and then taking the square root (typically referred to as "sum-of-squares" combination). The log of the ratio of these two echo time images (SOS_TE1 and SOS_TE2) was calculated, and scaled by the echo time difference, to give the R2*. T2* is calculated as the inverse of R2*. The T2* image is then spatially filtered (3x3x1 median filtering followed by limited dilation to fill missing data holes) to reduce noise (resulting in T2star), and transformed into the space of the T1 (via registration of the bias-field-normalised magnitude image SWI_TOTAL_MAG), the resulting image being T2star_to_T1.

Quantitative susceptibility mapping (QSM) was performed using the phase data. First, individual channel phase images for each echo are combined using the MCPC-3D-S approach (resulting in PHASE_TE1 and PHASE_TE2) [Eckstein et al., 2018] and unwrapped using a Laplacian-based algorithm [Schofield and Zhu, 2003], and the two echoes are combined with weighted averaging [Wu et al., 2012]. Brain-edge voxels with extremely large phase variance (primarily near sinuses) are detected and excluded [Wang et al., 2022]. Background fields are removed using the variable kernel sophisticated harmonic artifact reduction for phase data (V-SHARP) algorithm (resulting in filtered_phase_VSHARP) [Schweser et al., 2011]. Finally, χ maps are calculated using iLSQR (resulting in QSM) [Li et al., 2015] and referenced to cerebrospinal fluid (CSF) in the lateral ventricles (resulting in QSM_CSFref). Files for transforming QSM maps into T1 or MNI-standard space can be easily generated and applied.

3.9 B0 fieldmap processing

The B0 fieldmap-related pipeline outputs are in folder fieldmap (although these are derived primarily from the dMRI data).

All b=0 dMRI images with opposite phase-encoding direction (anterior-posterior (AP) and posterior-anterior (PA)) are analysed, to identify the highest-quality pair of AP and PA images. This optimal AP/PA pair is then fed into Topup http://fsl.fmrib.ox.ac.uk/fsl/fslwiki/TOPUP [Andersson et al., 2003] in order to estimate the B0 fieldmap and associated dMRI EPI distortions. GDC is then applied.

The EPI distortion information needed by the remaining dMRI processing is saved in files fieldmap_out_fieldcoef.nii.gz and fieldmap_out_movpar.txt.

The magnitude image is then linearly aligned to the T1, for later use in unwarping the fMRI data; the resulting transformation is the applied to the fieldmap, resulting in the T1-space fieldmap fieldmap_fout_to_T1_brain_rad.

3.10 dMRI processing

The original dMRI data and processing pipeline outputs are in folder dMRI. The raw data is in folder dMRI/raw, which contains the primary data used for diffusion analyses (AP), along with associated b value and vector text files, and the 3 b=0 phase-reversed images (PA).

First the data is corrected for eddy currents and head motion, and has outlier-slices (individual slices in the 4D data) corrected, using the Eddy tool http://fsl.fmrib.ox.ac.uk/fsl/fslwiki/EDDY [Andersson and Sotiropoulos, 2015, Andersson and Sotiropoulos, 2016]. GDC is then applied, resulting in the 4D output file dMRI/data_ud.

This is then fed into two complementary analyses, one based on tract-skeleton processing, and the other based on a richer modelling of within-voxel tract structure, followed by probabilistic tractography analysis (BEDPOSTx / PROBTRACKx). Both analysis streams then report a range of dMRI-derived measures within different tract regions: A) measures derived from diffusion-tensor modelling, and B) measures derived from microstructural model fitting. Outputs from both these modellings are in the dMRI subfolder.

The b=1000 shell (50 directions) is fed into the diffusion-tensor-imaging (DTI) fitting tool DTIFIT, creating DTI outputs such as fractional anisotropy dMRI/dti_FA, tensor mode dMRI/dti_MO and mean diffusivity dMRI/dti_MD.

In addition to the DTI fitting, the dMRI data is fed into NODDI (Neurite Orientation Dispersion and Density Imaging) modelling, using the AMICO (Accelerated Microstructure Imaging via Convex Optimization) tool https://github.com/daducci/AMICO [Zhang et al., 2012, Daducci et al., 2015]. This aims to generate meaningful voxelwise microstructural parameters, including ICVF (intra-cellular volume fraction - an index of white matter neurite density), ISOVF (isotropic or free water volume fraction) and OD (orientation dispersion index, a measure of within-voxel tract disorganisation).

3.10.1 TBSS-style analysis

The DTI FA image is then fed into TBSS (Tract-Based Spatial Statistics [Smith et al., 2006]), which aligns the FA image onto a standard-space white-matter skeleton, with alignment improved over the original TBSS skeleton-projection methodology through utilisation of a high-dimensional FNIRT-based warping [de Groot et al., 2013]. The resulting standard-space warp (TBSS/FA/dti_FA_to_MNI_warp) is applied to all other DTI/NODDI outputs. The final skeleton-space outputs are in TBSS/stats/all_*_skeletonised, where * represents each of the DTI and NODDI outputs (FA, etc). For each of the DTI/NODDI outputs, these skeletonised images are averaged across a set of 48 standard-space tract masks defined by the group of Susumi Mori at Johns Hopkins University [Mori et al., 2005, Wakana et al., 2007], similar to the processing applied in the ENIGMA project http://enigma.ini.usc.edu/protocols/dti-protocols.

3.10.2 Probabilistic-tractography-based analysis

Separately from the tensor/TBSS analysis, the Eddy output data is also fed into tractography-based analysis. This begins with within-voxel modelling of multi-fibre tract orientation structure via the BEDPOSTx tool (Bayesian Estimation of Diffusion Parameters Obtained using Sampling Techniques) http://fsl.fmrib.ox.ac.uk/fsl/fslwiki/FDT/UserGuide followed by probabilistic tractography (with crossing fibre modelling) using PROBTRACKx [Behrens et al., 2003, Behrens et al., 2007, Jbabdi et al., 2012]. The BEDPOSTx outputs are in folder dMRI.bedpostX; for example, the posterior mean fractional voxel occupancy for the principle fibre is mean_f1samples and the posterior mean direction of this fibre is dyads1. The BEDPOSTx outputs are suitable for running tractography from any (voxel or region) seeding; the pipeline has already automatically mapped a set of 27 major tracts using standard-space start/stop ROI masks defined by AutoPtx http://fsl.fmrib.ox.ac.uk/fsl/fslwiki/AutoPtx [de Groot et al., 2013]. Although the Eddy and BEDPOSTx outputs are in the space and resolution of the (GDC-unwarped) native diffusion data space, the nonlinear transformation between this space

and 1mm MNI standard space (as estimated by TBSS above) is used to create tractography results in 1mm standard space. PROBTRACKx outputs are in autoptx_preproc/tracts. For each tract, and for each DTI/NODDI output image type, an IDP is generated - the weighted-mean value of the DTI/NODDI parameter within the tract (the weighting being determined by the tractography output).

3.11 rfMRI processing

The rfMRI data and processing outputs are in folder fMRI; the raw (original) timeseries data is rfMRI and the single-band (single timepoint) reference scan is rfMRI_SBREF.

The processed rfMRI data is in folder rfMRI.ica. The following pre-processing was applied: motion correction using MCFLIRT [Jenkinson et al., 2002]; grand-mean intensity normalisation of the entire 4D dataset by a single multiplicative factor; highpass temporal filtering (Gaussian-weighted least-squares straight line fitting, with sigma=50.0s); EPI unwarping (utilising the fieldmaps as described above); GDC unwarping. Finally, structured artefacts are removed by ICA+FIX processing (Independent Component Analysis followed by FMRIB's ICA-based X-noiseifier [Beckmann and Smith, 2004, Salimi-Khorshidi et al., 2014, Griffanti et al., 2014]). FIX was hand-trained on 40 Biobank rfMRI datasets, and leave-one-out testing showed (mean/median) 99.1/100.0% classification accuracy for non-artefact components and 98.1/98.3% accuracy for artefact components. The final pre-processed rfMRI timeseries data is filtered_func_data_clean. At this point no lowpass temporal or spatial filtering has been applied.

The EPI unwarping is a combined step that also includes alignment to the T1, though the unwarped data is written out in native (unwarped) fMRI space (and the transform to T1 space written out separately). This T1 alignment is carried out by FLIRT, with a final BBR cost function [Greve and Fischl, 2009]. After the fMRI GDC unwarping, a final FLIRT realignment to T1 is applied, to take into account any shifts resulting from the GDC unwarping. The previously described transform from T1 space to standard MNI space is utilised when fMRI data is needed in standard space.

A group-average RSN (resting-state network) analysis was carried out using 4100 datasets. First, each timeseries dataset was temporally demeaned and had variance normalisation applied according to [Beckmann and Smith, 2004]. Group-PCA output was generated by MIGP (MELODIC's Incremental Group-PCA) from all subjects. This comprises the top 1200 weighted spatial eigenvectors from a group-averaged PCA (a very close approximation to concatenating all subjects' timeseries and then applying PCA) [Smith et al., 2014]. The MIGP output was fed into group-ICA using FSL's MELODIC tool [Hyvärinen, 1999, Beckmann and Smith, 2004], applying spatial-ICA at two different dimensionalities (25 and 100). The dimensionality determines the number of distinct ICA components; a higher number means that the above-threshold regions within the spatial component maps will be smaller. The group-ICA spatial maps are available at http://biobank.ctsu.ox.ac.uk/crystal/refer.cgi?id=9028 and also at (with online visualisation) http://www.fmrib.ox.ac.uk/ukbiobank. The sets of ICA maps can be considered as "parcellations" of (cortical and sub-cortical) grey matter, though they lack some properties often assumed for parcellations - for example, ICA maps are not binary masks but contain a continuous range of values; they can overlap each other; and a given map can include multiple spatially separated peaks/regions. Any group-ICA components that are clearly identifiable as artefactual (i.e., not neuronally driven) are discarded during the network modelling described below; a text file is supplied with the group-ICA maps, listing the group-ICA components kept in the final network modelling.

For a given parcellation (group-ICA decomposition of D components), the set of ICA spatial maps was mapped onto each subject's rfMRI timeseries data to derive one representative timeseries per ICA component (for these purposes each ICA component is considered as a network "node"). For each subject, these D timeseries can then be used in network analyses, described below. This is the first stage in a dual-regression analysis [Filippini et al., 2009]. The single-subject node timeseries are in subfolders rfMRI_*.dr (where * is the dimensionality).

The node timeseries are then used to estimate subject-specific network-matrices (also referred to as "netmats" or "parcellated connectomes"). For each subject, the D node-timeseries were fed into network modelling, discarding the clearly artefactual parcels (nodes), leaving D' nodes. This results in a D'xD' matrix of connectivity estimates. Network modelling was carried out using the FSLNets toolbox http://fsl.fmrib.ox.ac.uk/fsl/fslwiki/FSLNets. Network modelling is applied in two ways: 1. Using full normalized temporal correlation between every node timeseries and every other. This is a common approach and is very simple, but it has various practical and interpretational disadvantages including an inability to differentiate between directly connected nodes and

nodes that are only connected via an intermediate node [Smith, 2012]. 2. Using partial temporal correlation between nodes' time-series. This aims to estimate direct connection strengths better than achieved by full correlation. To slightly improve the estimates of partial correlation coefficients, L2 regularization is applied (setting rho=0.5 in the Ridge Regression netmats option in FSLNets). Netmat values were Gaussianised from Pearson correlation scores (r-values) into z-statistics, including empirical correction for temporal autocorrelation. Group-average netmats are available at http://biobank.ctsu.ox.ac.uk/crystal/refer.cgi?id=9028.

3.12 tfMRI processing

The tfMRI data and processing outputs are in folder fMRI; the raw timeseries data is tfMRI and the single-band (single timepoint) reference scan is tfMRI_SBREF.

The processed tfMRI data is in folder tfMRI.feat. The same pre-processing and registration was applied as for the rfMRI described above, except that spatial smoothing (using a Gaussian kernel of FWHM 5mm) was applied before the intensity normalisation, and no ICA+FIX artefact removal was run. The final pre-processed tfMRI timeseries data is filtered_func_data.

Task-induced activation modelling was carried out using FEAT (FMRI Expert Analysis Tool); time-series statistical analysis was carried out using FILM with local autocorrelation correction [Woolrich et al., 2001]. The timings of the blocks of the two task conditions (shapes and faces) are defined in text files custom_timing_files/ev1.txt and custom_timing_files/ev2.txt. 5 activation contrasts were defined (Shapes, Faces, Shapes+Faces, Shapes-Faces, Faces-Shapes), and an f-contrast also applied across Shapes and Faces.

The 3 contrasts of most interest are: 1 (Shapes), 2 (Faces) and 5 (Faces-Shapes), with the last of those being of particular interest with respect to amygdala activation. Group-average activation maps were derived from analysis across all subjects, and used to define ROIs for generating tfMRI IDPs. Four ROIs were derived; 1 (Shapes group-level fixed-effect z-statistic, thresholded at Z>120); 2 (Faces group-level fixed-effect z-statistic, thresholded at Z>120); 5 (Faces-Shapes group-level fixed-effect z-statistic, thresholded at Z>120); 5a (Faces-Shapes group-level fixed-effect z-statistic, thresholded at Z>120, and further masked by an amygdala-specific mask). The group-average activation maps and ROIs are available http://biobank.ctsu.ox.ac.uk/crystal/refer.cgi?id=9028.

The Featquery tool was used to extract summary statistics for the 3 main contrasts, for both activation effect size (expressed as a % signal change relative to the overall-image-mean baseline level) and statistical effect size (z-statistic), with each of these summarised across the relevant ROI in two ways - median across ROI voxels and 90th percentile across ROI voxels.

Display of the task video and logging of participant responses is carried out by ePrime software, which provides several response log files from each subject. These are not used in the above analyses (as the timings of the task blocks are fixed and already known, and the correctness of subject responses are not used in the above analyses), but are available in the UK Biobank database.

3.13 ASL processing

The ASL data and processing outputs are in the folder ASL. The raw, unprocessed data can be found in the raw subfolder, in which there is a separate NIFTI file for each postlabelling delay for both control and label conditions, as well as the M0 (calibration) volume. The scanner also saves out images that have had the prescan normalise correction applied to remove the effect of the receive coil non-uniformity (ASL_M0_NORM.nii.gz and all the files in the NORM subfolder), as well as the absolute difference between control and label volumes (in the DIFF subfolder). The NORM and DIFF data are not currently used in the processing pipeline, but are included in case others wish to process data in a different way.

Processed data can be found in the BASIL subfolder. The raw label and control images are merged into a single file (ASL_DATA), then the data are passed into the oxford_asl tool https://fsl.fmrib.ox.ac.uk/fsl/fslwiki/oxford_asl [Chappell et al., 2009]. This includes motion correction with MCFLIRT (https://fsl.fmrib.ox.ac.uk/fsl/fslwiki/MCFLIRT), combined gradient distortion and B0 distortion correction using the fieldmap derived from the blip-reversed b0 diffusion data, pairwise subtraction of control and label data at each postlabelling delay, linear registration to the T1 structural image with FLIRT (https://fsl.fmrib.ox.ac.uk/fsl/fslwiki/FLIRT) and kinetic model fitting using the variational Bayesian model fitting tool

FABBER (https://fsl.fmrib.ox.ac.uk/fsl/fslwiki/FABBER). The general kinetic model for ASL [Buxton et al., 1998] is used, accounting for a macrovascular component [Chappell et al., 2010], with a spatial prior being used to regularise the fitting [Groves et al., 2009]. This results in CBF (perfusion), ATT (arrival) and macrovascular blood volume (aCBV) maps, along with the variance in these estimates (files with _var in the filename), which can be found in BASIL/OXASL_ra_dir/native_space/. At this stage, the CBF and aCBV maps are in arbitrary units.

A voxelwise calibration procedure is then performed, using the calibration (M0) image corrected for the difference in image scaling to the main ASL data (a factor of 10), the inversion efficiency of PCASL (assumed to be 0.85) and the partition coefficient (assumed to be 0.9). Median smoothing, erosion and extrapolation are used to produce more robust M0 estimates at the edges of the brain. Division by this M0 image then allows perfusion, aCBV and their associated variance maps to be calculated in absolute units: perfusion_calib in ml/100g/min and aCBV_calib in %, which are also found in the native_space subfolder. The equivalent maps co-registered into the subject's structural space or standard space can be found in the struct_space and std_space subdirectories, respectively.

Mean, standard deviation, median, interquartile range and precision-weighted mean CBF and ATT values within various ROIs are also automatically calculated and saved in the region_analysis subfolder. The full ASL pipeline can be found at https://git.fmrib.ox.ac.uk/falmagro/uk_biobank_pipeline_v_1.5/-/tree/master/bb_asl_pipeline

4 UK Biobank database ("Showcase") variables

In addition to the raw and processed "bulk" image data files available from UK Biobank, there are a number of derived numerical measures available as standalone variables available in the database (i.e., these are summary numbers rather than images). This includes QC (quality control) measures (such as overall signal-to-noise ratio for individual modalities), IDPs (imaging-derived phenotypes, such as total brain volume and left hippocampus volume) and other variables that are not QC or IDPs, but which may be useful as "confound" variables (for example, whether the FreeSurfer processing used the T2_FLAIR image in addition to the T1). These are now briefly described.

4.1 QC measures

All QC measures are designed such that "higher is worse". Some or all of these may be useful as confound covariates.

Several QC measures describe the "discrepancy" (generalised difference) between a given pair of images after they have been aligned together. Here a poor (large) score could arise either because the quality of the alignment is bad, or because one of the two images being compared is corrupted in some way. Two of these QC measures quantitate the discrepancy between the T1 structural image and the standard (population average) template image - one after a linear alignment (which cannot correct for the fine-detailed differences between a given subject and the population average), and the other after a nonlinear alignment (which should achieve much better correspondence). Related to this, the overall amount of nonlinear warping necessary to achieve a detailed alignment to the standard template is summarised as one QC measure. Finally, several other QC measures describe the discrepancy between the T1 image (for a given subject) and each of the other modalities (for that same subject), after linear alignment of the other modalities to the T1. All of these "discrepancy" QC measures are the unitless "correlation ratio" cost function, that is used by FLIRT to optimise alignments, and which is used here to quantify the discrepancy between any two images.

Several other QC measures quantitate signal to noise ratio (SNR) in some of the modalities. For the T1, the tissue-type segmentation is used to estimate within-tissue-type noise level (standard deviation), as well as mean intensities for grey and white matter. These quantities are used to estimate overall image SNR and also CNR (contrast to noise - white-grey mean intensity difference normalised by noise level). In both cases these measures are inverted before being recorded as QC measures, so that "higher is worse". From the preprocessed rfMRI (both before and after artefact removal) and tfMRI timeseries data, similar measures are calculated, but in this case the "noise" level is the temporal standard deviation. First, voxelwise SNR is calculated, and then the median (across brain voxels) estimated. This is then inverted for the reported QC measure.

Also from the rfMRI and tfMRI data, the total amount of head motion is summarised as additional QC measures. For each consecutive pair of timepoints, the mean displacement (averaged across the brain) is estimated, and this is then averaged across all timepoints.

Finally, from the dMRI data, the total number outlier slices (from all slices in all dMRI volumes) is reported, as output by the Eddy tool. This is mostly reflective of head motion during the dMRI scan.

4.2 Additional head motion variables

In addition to the simple fMRI head motion variables listed above, we compute a range of additional motion-related variables.

As described in [Alfaro-Almagro et al., 2021], we obtained the motion estimates from FSL's FEAT [Woolrich et al., 2001] and Eddy [Andersson et al., 2016, Andersson et al., 2017], and estimated the mean, median and 90th percentile over time of the absolute and relative motion in the tfMRI, rfMRI, and dMRI. We also included (as a confound) the number of slices that Eddy estimated to be outliers in the dMRI data (because of significant signal dropout which is largely due to motion).

A second approach has been to calculate the same quantile summaries (mean, median and 90th percentile) of the motion over space and time calculated from FSL's FEAT motion estimation matrices from resting fMRI in a similar way as described in [Satterthwaite et al., 2013]. These might capture additional useful motion-related confound information given that the amount of motion varies across both space and time in general.

Further motion-related variables are estimated via the DVARS approach. We included the mean, median and 90th percentile over time of S-var and D-var normalised by A-var (variants of DVARS (Afyouni and Nichols, 2018)) from both the original resting fMRI, and the resting fMRI after removal of noise components using FIX [Griffanti et al., 2014, Griffanti et al., 2017].

Finally, an estimate of structural (T1) head motion [Alfaro-Almagro et al., 2021] is calculated by fitting a cross-validated linear regression, where the dependent variable was a manually evaluated QC measure of motion in 871 T1w images, and the independent variables were a set of features that are related to structural motion and QC (smoothness estimates in X, Y, and Z [Flitney and Jenkinson, 2000], average Euler number of the FreeSurfer surfaces [Rosen et al., 2018] and Qoala-T quality metric of FreeSurfer output [Klapwijk et al., 2019].

4.3 Other confound-regressor variables

In addition to some QC variables, there are several other variables that are likely to be useful as "confound variables" when working with UKB imaging data. A detailed paper on UKB confounds will be published shortly.

Scanning centre (site)

Data-Field 54 can be used to identify the imaging centre, in case there is any site-specific variability in the imaging (though initial testing has suggested that there is not large site variability): `http://biobank.ctsu.ox.ac.uk/showcase/field.cgi?id=54`

For example one might derive a binary indicator confound variable for each site).

Subject's head size

In general IDPs are not normalised for brain or head size (except for the few SIENAX measures that explicitly state that they are normalised in their summary descriptions). If it is desired to normalise an IDP for head size, the T1-based "headsize scaling factor" (`http://biobank.ctsu.ox.ac.uk/crystal/field.cgi?id=25000`) should be used. Note that this is the scaling factor estimated when transforming from native to standard space, so to normalise variables for head size, one should *multiply* raw IDP values by this (not divide).

It is important to note that in general it is only sensible to scale IDPs by this head size scaling factor when the IDP in question is a raw volumetric measure. For other types of IDP, normalising by this non-demeaned head size scaling variable is likely to *induce* head size confounds into the data (this is similar to the danger of inducing confound effects when regressing out confounds that have not been demeaned). In general, the safer way to approach deconfounding is to regress out demeaned confound regressors.

Location of head in scanner

Additionally, the exact location of the head and the radio-frequency receive coil in the scanner can affect data quality and imaging-derived phenotypes. To help account for variations in position in different scanned participants, several variables have been generated which describe aspects of the positioning and can be used as "confounding variables" - for example they might be regressed out of brain phenotypes before carrying out correlations between these and non-imaging variables. The relevant variables are:

- Data-Field 25756: X-position of centre-of-gravity of brain mask in scanner co-ordinates
- Data-Field 25757: Y-position of back of brain mask in scanner co-ordinates
- Data-Field 25758: Z-position of centre-of-gravity of brain mask in scanner co-ordinates
- Data-Field 25759: Z-position of table/coil in scanner co-ordinates

Minor prototol parameter variations and scanner drift

A few minor protocol parameter changes have been made in error at the imaging sites for some subjects, in the process of distributing the protocol across sites (fMRI echo times of 42.4 vs 39ms, and overall global intensity scaling of images). These have been investigated, and none of them has a large effect on imaging data or derived IDPs, but several additional confound variables have been generated to help minimise additional uncontrolled data variance.

Separately, it has become clear that there have been slowly-changing heating-related effects in the extent of eddy currents in the dMRI data. This effect is now regularly checked for, and the scanner recalibrated when appropriate, but it was necessary for affected datasets to have a more robust version of eddy current correction applied (primarily by increasing the search space for eddy currents). Two new confound variables reflecting this effect have been created.

The additional confounds are:

Code	Short name	Modality	Description
25921	NewEddy	dMRI	Whether increased search space in eddy current estimation was used for dMRI
25922	YTranslation	dMRI	Standard deviation of apparent translation in the Y axis as measured by eddy
25923	TErfMRI	rfMRI	Echo Time for the rfMRI
25924	TEtfMRI	tfMRI	Echo Time for the tfMRI
25925	T1Scaling	T1	Intensity scaling for T1
25926	T2FLAIRScaling	T2	Intensity scaling for T2_FLAIR
25927	SWIScaling	SWI	Intensity scaling for SWI
25928	dMRIScaling	dMRI	Intensity scaling for dMRI
25929	rfMRIScaling	rfMRI	Intensity scaling for rfMRI
25930	tfMRIScaling	tfMRI	Intensity scaling for tfMRI

Other confounds

Other possibly useful confound variables include the summary fMRI head motion variables, number of dMRI outlier slices, and whether T2_FLAIR was used with T1 for FreeSurfer. Additionally, subject-specific measures such as sex and age, and possible body-size-related variables such as height, weight and BMI, might be considered confound variables, although of course such confounds may also relate to effects of interest [Smith and Nichols, 2018]. Additionally variables such as "Discrepancy between T1 brain image and standard-space brain template (linearly-aligned)" (25731) might be useful confound variables, but might also reflect pathology or aging processes, and so could remove variance of interest.

4.4 IDPs

IDPs are designed such that each different IDP aims to describe one single objective and meaningful quantity in the brain imaging data, from simple global IDPs such as total brain volume, to highly specific, spatially-focal IDPs such as the mean white matter fractional anisotropy in the left uncinate fasciculus.

From the T1 structural image, several global volume measures are reported as distinct IDPs, both normalised for overall head size as well as not normalised: total brain (grey + white matter) volume; total white matter volume, total grey matter volume, ventricular (non-peripheral) CSF (cerebrospinal fluid) volume; peripheral cortical grey matter volume. Also the overall volumetric head-size scaling factor is recorded as an IDP. The total "regional" grey matter volume is estimated in 139 different regions-of-interest defined from atlases in standard space. Finally, from the T1, several subcortical structures' volumes (not normalised for brain/head size) are reported, in general with separate IDPs for left and right, such as left thalamus and right thalamus. Many additional IDPs are created via FreeSurfer processing, as described above.

From the T2_FLAIR (combined with T1) data, white matter lesions are estimated, and an IDP is created as the total volume across all lesions.

From the SWI data, T2* and QSM images are estimated. The median (across ROI voxels) T2* and magnetic susceptibility values are then estimated as a separate IDP for each of the subcortical structure ROIs (left thalamus, right caudate, etc.) estimated from the T1. Additional IDPs for (left and right) substantia nigra are estimated based on an MNI atlas for substantia nigra.

From the tfMRI data, activation is estimated for the 3 primary "contrasts" of interest (as described above). For these contrasts ("Shapes", "Faces" and "Faces-Shapes"), a population-average activation was estimated and used to define a region-of-interest (ROI) within which to estimate subject-specific activation IDPs. Across voxels in the relevant ROI, the median and 90th percentile activation are estimated for each contrast, reporting both activation effect size (expressed as a % signal change relative to the overall-image-mean baseline level) and statistical effect size (z-statistic). The third contrast ("Faces-Shapes") was also evaluated within an additional group-defined ROI - the intersection of the original group-average ROI for this contrast, and an amygdala

mask derived from the Harvard-Oxford structural atlas.

From the rfMRI data, the group-average data was "parcellated" into areas at two different levels of detail (D=25 parcels spanning the brain and, separately, D=100). As described in more detail above, these parcellations were then mapped onto individual subjects' datasets, and clearly-artefactual parcels discarded, resulting in D'xD' network models (matrices) for each subject. As the matrices are symmetric, only values above the diagonal are kept, and unwrapped into a single row of (D' x (D'-1) / 2) values per subject. This results in one "compound" IDP (containing all network matrix values for a given subject) for each original dimensionality (D=25 and 100) and for each network matrix estimation method (full correlation and partial correlation). Further IDPs are estimated as the fluctuation amplitudes (node temporal standard deviation) for each of the nodes, from both dimensionalities.

Spatially-specific IDPs related to the dMRI data are derived in two different ways, as mentioned above in the processing pipeline descriptions. All diffusion tensor imaging (DTI) measures (such as FA) and microstructural NODDI measures are summarised as averaged in specific areas/tracts. In the first set of measurements, the diffusion data is aligned to a white-matter tract skeleton, and the DTI/NODDI measures averaged within 48 distinct tract ROIs defined using the Johns Hopkins University tract atlas. In the second set of measurements, probabilistic tractography is run using a set of standard space seed/termination masks, and DTI/NODDI measures averaged within 27 distinct tracts' maps.

From the ASL data, precision-weighted mean CBF and ATT estimates are provided within a range of different ROIs. These include the right and left frontal, occipital, parietal and temporal lobes and cerebellum within a grey matter mask (>10% grey matter partial volume) where the ASL signal is most robust. Similar measures are also extracted within vascular territory masks derived from a manually drawn atlas (http://dx.doi.org/10.6084/m9.figshare.1488674): the right and left internal carotid artery and the vertebrobasilar arteries, eroded slightly to avoid overlap and reduce sensitivity to slight mis-registration. "Purer" measures of whole brain or cortical grey matter CBF and ATT are also calculated using a stricter grey matter partial volume threshold (>70%, since a higher threshold would result in few voxels remaining at the course resolution of the ASL data). ASL is less reliable in the white matter, so larger ROIs were used to improve robustness: relatively pure (>90% partial volume) white matter in the whole brain and just the cerebrum, and slightly less restrictive right and left cerebrum (>80% partial volume, which still results in a large number of voxels within the mask due to greater dimensions of white matter regions). Through-slice blurring that results from the use of a 3D-GRASE readout means there may be some significant contamination of white matter IDPs by neighbouring grey matter, so results should be interpreted with caution.

References

[Alfaro-Almagro et al., 2018] Alfaro-Almagro, F., Jenkinson, M., Bangerter, N., Andersson, J., Griffanti, L., Douaud, G., Sotiropoulos, S., Jbabdi, S., Hernandez-Fernandez, M., Valee, E., Vidaurre, D., Webster, M., McCarthy, P., Rorden, C., Daducci, A., Alexander, D., Zhang, H., Dragonu, I., Matthews, P., Miller, K., and Smith, S. (2018). Image processing and quality control for the first 10,000 brain imaging datasets from UK Biobank. *NeuroImage*, 166:400–424.

[Alfaro-Almagro et al., 2021] Alfaro-Almagro, F., McCarthy, P., Afyouni, S., Andersson, J. L., Bastiani, M., Miller, K. L., Nichols, T. E., and Smith, S. M. (2021). Confound modelling in UK Biobank brain imaging. *NeuroImage*, page 117002.

[Andersson et al., 2007a] Andersson, J., Jenkinson, M., and Smith, S. (2007a). Non-linear registration aka spatial normalisation. Internal Technical Report TR07JA2, Oxford Centre for Functional Magnetic Resonance Imaging of the Brain, Department of Clinical Neurology, Oxford University, Oxford, UK. Available at `www.fmrib.ox.ac.uk/analysis/techrep` for downloading.

[Andersson et al., 2003] Andersson, J., Skare, S., and Ashburner, J. (2003). How to correct susceptibility distortions in spin-echo echo-planar images: application to diffusion tensor imaging. *Neuroimage*, 20(2):870–888.

[Andersson et al., 2007b] Andersson, J., Smith, S., and Jenkinson, M. (2007b). Non-linear optimisation. Internal Technical Report TR07JA1, Oxford Centre for Functional Magnetic Resonance Imaging of the Brain, Department of Clinical Neurology, Oxford University, Oxford, UK. Available at `www.fmrib.ox.ac.uk/analysis/techrep` for downloading.

[Andersson and Sotiropoulos, 2015] Andersson, J. and Sotiropoulos, S. (2015). Non-parametric representation and prediction of single- and multi-shell diffusion-weighted mri data using Gaussian processes. *NeuroImage*, 122:166–176.

[Andersson and Sotiropoulos, 2016] Andersson, J. and Sotiropoulos, S. (2016). An integrated approach to correction for off-resonance effects and subject movement in diffusion MR imaging. *NeuroImage*, 125:1063–1078.

[Andersson et al., 2016] Andersson, J. L., Graham, M. S., Zsoldos, E., and Sotiropoulos, S. N. (2016). Incorporating outlier detection and replacement into a non-parametric framework for movement and distortion correction of diffusion mr images. *NeuroImage*, 141:556–572.

[Andersson et al., 2017] Andersson, J. L. R., Graham, M. S., Drobnjak, I., Zhang, H., Filippini, N., and Bastiani, M. (2017). Towards a comprehensive framework for movement and distortion correction of diffusion MR images: Within volume movement. *Neuroimage*, 152:450–466.

[Barch et al., 2013] Barch, D., Burgess, G., Harms, M., Petersen, S., Schlaggar, B., Corbetta, M., Glasser, M., Curtiss, S., Dixit, S., Feldt, C., Nolan, D., Bryant, E., Hartley, T., Footer, O., Bjork, J., Poldrack, R., Smith, S., Johansen-Berg, H., Snyder, A., and Van Essen, D. - for the WU-Minn HCP Consortium (2013). Function in the Human Connectome: Task-fMRI and individual differences in behavior. *NeuroImage*, 80:169–189.

[Beckmann and Smith, 2004] Beckmann, C. and Smith, S. (2004). Probabilistic independent component analysis for functional magnetic resonance imaging. *IEEE Trans. on Medical Imaging*, 23(2):137–152.

[Behrens et al., 2007] Behrens, T., Johansen-Berg, H., Jbabdi, S., Rushworth, M., and Woolrich, M. (2007). Probabilistic diffusion tractography with multiple fibre orientations. What can we gain? *NeuroImage*, 23:144–155.

[Behrens et al., 2003] Behrens, T., Woolrich, M., Jenkinson, M., Johansen-Berg, H., Nunes, R., Clare, S., Matthews, P., Brady, J., and Smith, S. (2003). Characterization and propagation of uncertainty in diffusion-weighted MR imaging. *Magn Reson Med*, 50(5):1077–1088.

[Buxton et al., 1998] Buxton, R. B., Frank, L. R., Wong, E. C., Siewert, B., Warach, S., and Edelman, R. R. (1998). A general kinetic model for quantitative perfusion imaging with arterial spin labeling. *Magnetic Resonance in Medicine*, 40(3):383–396. ISBN: 1522-2594.

[Chappell et al., 2009] Chappell, M., Groves, A., Whitcher, B., and Woolrich, M. (2009). Variational Bayesian Inference for a Nonlinear Forward Model. *IEEE Transactions on Signal Processing*, 57(1).

[Chappell et al., 2010] Chappell, M. A., MacIntosh, B. J., Donahue, M. J., Günther, M., Jezzard, P., and Woolrich, M. W. (2010). Separation of macrovascular signal in multi-inversion time arterial spin labelling MRI. *Magnetic Resonance in Medicine*, 63(5):1357–1365.

[Daducci et al., 2015] Daducci, A., Canales-Rodríguez, E. J., Zhang, H., Dyrby, T. B., Alexander, D. C., and Thiran, J.-P. (2015). Accelerated microstructure imaging via convex optimization (AMICO) from diffusion MRI data. *NeuroImage*, 105:32–44.

[Dale et al., 1999] Dale, A., Fischl, B., and Sereno, M. (1999). Cortical surface-based analysis I: Segmentation and surface reconstruction. *NeuroImage*, 9:179–194.

[de Groot et al., 2013] de Groot, M., Vernooij, M., Klein, S., Ikram, A., Vos, F., Smith, S., Niessen, W., and Andersson, J. (2013). Improving alignment in tract-based spatial statistics: evaluation and optimization of image registration. *NeuroImage*, 76:400–411.

[Desikan et al., 2006] Desikan, R., Segonne, F., Fischl, B., Quinn, B., Dickerson, B., Blacker, D., Buckner, R., Dale, A., Maguire, R., Hyman, B., Albert, M., and Killiany, R. (2006). An automated labeling system for subdividing the human cerebral cortex on MRI scans into gyral based regions of interest. *NeuroImage*, 31:968–980.

[Eckstein et al., 2018] Eckstein, K., Dymerska, B., Bachrata, B., Bogner, W., Poljanc, K., Trattnig, S., and Robinson, S. D. (2018). Computationally efficient combination of multi-channel phase data from multi-echo acquisitions (ASPIRE). *Magnetic Resonance in Medicine*, 79(6):2996–3006.

[Filippini et al., 2009] Filippini, N., MacIntosh, B., Hough, M., Goodwin, G., Frisoni, G., Smith, S., Matthews, P., Beckmann, C., and Mackay, C. (2009). Distinct patterns of brain activity in young carriers of the APOE-e4 allele. *Proc Natl Acad Sci USA (PNAS)*, 106:7209–7214.

[Fischl et al., 2002] Fischl, B., Salat, D., Busa, E., Albert, M., Dieterich, M., Haselgrove, C., van der Kouwe, A., Killiany, R., Kennedy, D., Klaveness, S., Montillo, A., Makris, N., Rosen, B., and Dale, A. (2002). Whole brain segmentation: Automated labeling of neuroanatomical structures in the human brain. *Neuron*, 33:341–355.

[Fischl et al., 1999a] Fischl, B., Sereno, M., and Dale, A. (1999a). Cortical surface-based analysis II: Inflation, flattening, and a surface-based coordinate system. *NeuroImage*, 9:195–207.

[Fischl et al., 1999b] Fischl, B., Sereno, M., Tootell, R., and Dale, A. (1999b). High-resolution intersubject averaging and a coordinate system for the cortical surface. *Human Brain Mapping*, 8(4):272–284.

[Fischl et al., 2004] Fischl, B., van der Kouwe, A., Destrieux, C., Halgren, E., Segonne, F., Salat, D., Busa, E., Seidman, L., Goldstein, J., Kennedy, D., Caviness, V., Makris, N., Rosen, B., and Dale, A. (2004). Automatically parcellating the human cerebral cortex. *Cerebral Cortex*, 14:11–22.

[Flitney and Jenkinson, 2000] Flitney, D. E. and Jenkinson, M. (2000). Cluster analysis revisited. In *Tech. rept. Oxford Centre for Functional Magnetic Resonance Imaging of the Brain, Department of Clinical Neurology, Oxford University, Oxford, UK. TR00DF1*, page 1. Oxford Centre for Functional Magnetic Resonance Imaging of the Brain, Department of Clinical Neurology, Oxford University, Oxford, UK.

[Greve and Fischl, 2009] Greve, D. and Fischl, B. (2009). Accurate and robust brain image alignment using boundary-based registration. *NeuroImage*, 48:63–72.

[Griffanti et al., 2017] Griffanti, L., Douaud, G., Bijsterbosch, J., Evangelisti, S., Alfaro-Almagro, F., Glasser, M. F., Duff, E. P., Fitzgibbon, S., Westphal, R., Carone, D., Beckmann, C. F., and Smith, S. M. (2017). Hand classification of fMRI ICA noise components. *Neuroimage*, 154:188–205.

[Griffanti et al., 2014] Griffanti, L., Salimi-Khorshidi, G., Beckmann, C., Auerbach, E., Douaud, G., Sexton, C., Zsoldos, E., Ebmeier, K., Filippini, N., Mackay, C., Moeller, S., Xu, J., Yacoub, E., Baselli, G., Ugurbil, K., Miller, K., and Smith, S. (2014). ICA-based artefact removal and accelerated fMRI acquisition for improved resting state network imaging. *NeuroImage*, 95:232–247.

[Griffanti et al., 2016] Griffanti, L., Zamboni, G., Khan, A., Li, L., Bonifacio, G., Sundaresan, V., Schulz, U., Kuker, W., Battaglini, M., Rothwell, P., and Jenkinson, M. (2016). BIANCA (Brain Intensity AbNormality Classification Algorithm): A new tool for automated segmentation of white matter hyperintensities. *NeuroImage*, 141:191–205.

[Groves et al., 2009] Groves, A. R., Chappell, M. A., and Woolrich, M. W. (2009). Combined spatial and non-spatial prior for inference on MRI time-series. *NeuroImage*, 45(3).

[Haacke et al., 2004] Haacke, E., Xu, Y., Cheng, Y., and Reichenbach, J. (2004). Susceptibility-weighted imaging (SWI). *Magnetic Resonance in Medicine*, 52:612–618.

[Hariri et al., 2002] Hariri, A. R., Tessitore, A., Mattay, V. S., Fera, F., and Weinberger, D. R. (2002). The amygdala response to emotional stimuli: a comparison of faces and scenes. *Neuroimage*, 17(1):317–323.

[Hyvärinen, 1999] Hyvärinen, A. (1999). Fast and robust fixed-point algorithms for independent component analysis. *IEEE Transactions on Neural Networks*, 10(3):626–634.

[Iglesias et al., 2015] Iglesias, J., Augustinack, J., Nguyen, K., Player, C., Player, A., Wright, M., Roy, N., Frosch, M., McKee, A., Wald, L., Fischl, B., and Van Leemput, K. (2015). A computational atlas of the hippocampal formation using ex vivo, ultra-high resolution MRI: Application to adaptive segmentation of in vivo MRI. *NeuroImage*, 115:117–137.

[Jbabdi et al., 2012] Jbabdi, S., Sotiropoulos, S. N., Savio, A. M., Grana, M., and Behrens, T. E. (2012). Model-based analysis of multishell diffusion MR data for tractography: How to get over fitting problems. *Magnetic Resonance in Medicine*, 68(6):1846–55.

[Jenkinson et al., 2002] Jenkinson, M., Bannister, P., Brady, J., and Smith, S. (2002). Improved optimisation for the robust and accurate linear registration and motion correction of brain images. *NeuroImage*, 17(2):825–841.

[Jenkinson et al., 2012] Jenkinson, M., Beckmann, C., Behrens, T., Woolrich, M., and Smith, S. (2012). FSL. *NeuroImage*, 62:782–790.

[Jenkinson and Smith, 2001] Jenkinson, M. and Smith, S. (2001). A global optimisation method for robust affine registration of brain images. *Medical Image Analysis*, 5(2):143–156.

[Klapwijk et al., 2019] Klapwijk, E., van de Kamp, F., van der Meulen, M., Peters, S., and Wierenga, L. M. (2019). Qoala-T: A supervised-learning tool for quality control of FreeSurfer segmented MRI data. *NeuroImage*, 189:116–129.

[Larkman et al., 2001] Larkman, D. J., Hajnal, J. V., Herlihy, A. H., Coutts, G. A., Young, I. R., and Ehnholm, G. (2001). Use of multicoil arrays for separation of signal from multiple slices simultaneously excited. *J Magn Reson Imaging*, 13(2):313–7.

[Li et al., 2015] Li, W., Wang, N., Yu, F., Han, H., Cao, W., Romero, R., Tantiwongkosi, B., Duong, T. Q., and Liu, C. (2015). A method for estimating and removing streaking artifacts in quantitative susceptibility mapping. *NeuroImage*, 108:111–122.

[Mennes et al., 2014] Mennes, M., Jenkinson, M., Valabregue, R., Buitelaar, J., Beckmann, C., and Smith, S. (2014). Optimizing full-brain coverage in human brain MRI through population distributions of brain size. *NeuroImage*, 98:513–520.

[Moeller et al., 2010] Moeller, S., Yacoub, E., Olman, C. A., Auerbach, E., Strupp, J., Harel, N., and Ugurbil, K. (2010). Multiband multislice GE-EPI at 7 tesla, with 16-fold acceleration using partial parallel imaging with application to high spatial and temporal whole-brain fMRI. *Magn Reson Med*, 63(5):1144–53.

[Mori et al., 2005] Mori, S., Wakana, S., van Zijl, P., and Nagae-Poetscher, L. (2005). *MRI Atlas of Human White Matter*. Elsevier.

[Patenaude et al., 2011] Patenaude, B., Smith, S., Kennedy, D., and Jenkinson, M. (2011). A Bayesian model of shape and appearance for subcortical brain segmentation. *NeuroImage*, 56(3):907–922.

[Pierpaoli and Basser, 1996] Pierpaoli, P. and Basser, P. (1996). Toward a quantitive assessment of diffusion anisotropy. *Magn. Reson. Med.*, 36:893–906.

[Rosen et al., 2018] Rosen, A. F., Roalf, D. R., Ruparel, K., Blake, J., Seelaus, K., Villa, L. P., Ciric, R., Cook, P. A., Davatzikos, C., Elliott, M. A., et al. (2018). Quantitative assessment of structural image quality. *Neuroimage*, 169:407–418.

[Salimi-Khorshidi et al., 2014] Salimi-Khorshidi, G., Douaud, G., Beckmann, C., Glasser, M., Griffanti, L., and Smith, S. (2014). Automatic denoising of functional MRI data: Combining independent component analysis and hierarchical fusion of classifiers. *NeuroImage*, 90:449–468.

[Satterthwaite et al., 2013] Satterthwaite, T. D., Elliott, M. A., Gerraty, R. T., Ruparel, K., Loughead, J., Calkins, M. E., Eickhoff, S. B., Hakonarson, H., Gur, R. C., Gur, R. E., and Wolf, D. H. (2013). An improved framework for confound regression and filtering for control of motion artifact in the preprocessing of resting-state functional connectivity data. *Neuroimage*, 64:240–256.

[Schofield and Zhu, 2003] Schofield, M. A. and Zhu, Y. (2003). Fast phase unwrapping algorithm for interferometric applications. *Opt. Lett.*, 28(14):1194–1196.

[Schweser et al., 2011] Schweser, F., Deistung, A., Lehr, B. W., and Reichenbach, J. R. (2011). Quantitative imaging of intrinsic magnetic tissue properties using MRI signal phase: An approach to in vivo brain iron metabolism? *NeuroImage*, 54(4):2789–2807.

[Smith, 2002] Smith, S. (2002). Fast robust automated brain extraction. *Human Brain Mapping*, 17(3):143–155.

[Smith, 2012] Smith, S. (2012). The future of FMRI connectivity. *NeuroImage*, 62:1257–1266.

[Smith et al., 2014] Smith, S., Hyvärinen, A., Varoquaux, G., Miller, K., and Beckmann, C. (2014). Group-PCA for very large fMRI datasets. *NeuroImage*, 101:738–749.

[Smith et al., 2006] Smith, S., Jenkinson, M., Johansen-Berg, H., Rueckert, D., Nichols, T., Mackay, C., Watkins, K., Ciccarelli, O., Cader, M., Matthews, P., and Behrens, T. (2006). Tract-based spatial statistics: Voxelwise analysis of multi-subject diffusion data. *NeuroImage*, 31:1487–1505.

[Smith et al., 2015] Smith, S., Kindlmann, G., and Jbabdi, S. (2015). Tract-based spatial statistics and other approaches for cross-subject comparison of local diffusion MRI parameters. In Toga, A., editor, *Brain Mapping: An Encyclopedic Reference*. Academic Press: Elsevier.

[Smith and Nichols, 2018] Smith, S. and Nichols, T. (2018). Statistical challenges in "big data" human neuroimaging. *Neuron*, 97:263–268.

[Smith et al., 2002] Smith, S., Zhang, Y., Jenkinson, M., Chen, J., Matthews, P., Federico, A., and De Stefano, N. (2002). Accurate, robust and automated longitudinal and cross-sectional brain change analysis. *NeuroImage*, 17(1):479–489.

[Ugurbil et al., 2013] Ugurbil, K., Xu, J., Auerbach, E., Moeller, S., Vu, A., Duarte-Carvajalino, J., Lenglet, C., Wu, X., Schmitter, S., Van de Moortele, P., Strupp, J., Sapiro, G., De Martino, F., Wang, D., Harel, N., Garwood, M., Chen, L., Feinberg, D., Smith, S., Miller, K., Sotiropoulos, S., Jbabdi, S., Andersson, J., Behrens, T., Glasser, M., Van Essen, D., and Yacoub, E. - for the WU-Minn HCP Consortium (2013). Pushing spatial and temporal resolution for functional and diffusion MRI in the Human Connectome Project. *NeuroImage*, 80:80–104.

[von Samson-Himmelstjerna et al., 2016] von Samson-Himmelstjerna, F., Madai, V. I., Sobesky, J., and Guenther, M. (2016). Walsh-ordered hadamard time-encoded pseudocontinuous ASL (WH pCASL): Walsh-Ordered Hadamard Time-Encoded pCASL. *Magnetic Resonance in Medicine*, 76(6):1814–1824.

[Wakana et al., 2007] Wakana, S., Caprihan, A., Panzenboeck, M., Fallon, J., Perry, M., Gollub, R., Hua, K., Zhang, J., Jiang, H., Dubey, P., Blitz, A., van Zijl, P., and Mori, S. (2007). Reproducibility of quantitative tractography methods applied to cerebral white matter. *NeuroImage*, 36(3):630–644.

[Wang et al., 2022] Wang, C., Martins-Bach, A. B., Alfaro-Almagro, F., Douaud, G., Klein, J. C., Llera, A., Fiscone, C., Bowtell, R., Elliott, L. T., Smith, S. M., Tendler, B. C., and Miller, K. L. (2022). Phenotypic and genetic associations of quantitative magnetic susceptibility in UK Biobank brain imaging. *Nature Neuroscience*, 25(6):818–831.

[Woolrich et al., 2001] Woolrich, M., Ripley, B., Brady, J., and Smith, S. (2001). Temporal autocorrelation in univariate linear modelling of FMRI data. *NeuroImage*, 14(6):1370–1386.

[Wu et al., 2012] Wu, B., Li, W., Avram, A. V., Gho, S.-M., and Liu, C. (2012). Fast and tissue-optimized mapping of magnetic susceptibility and T2* with multi-echo and multi-shot spirals. *NeuroImage*, 59(1):297–305. Neuroergonomics: The human brain in action and at work.

[Zhang et al., 2012] Zhang, H., Schneider, T., Wheeler-Kingshott, C. A., and Alexander, D. C. (2012). NODDI: practical in vivo neurite orientation dispersion and density imaging of the human brain. *Neuroimage*, 61(4):1000–1016.

[Zhang et al., 2001] Zhang, Y., Brady, M., and Smith, S. (2001). Segmentation of brain MR images through a hidden Markov random field model and the expectation maximization algorithm. *IEEE Trans. on Medical Imaging*, 20(1):45–57.

A Glossary

BOLD Blood-oxygen-level dependent MRI contrast - the signal in fMRI that is sensitive to changes in oxygenation level in the blood, and hence a marker for local grey matter activation.

z-statistic a test statistic (e.g., Pearson's r or t from a t-test) that has been transformed to be Gaussian (with mean 0, standard deviation 1) in the null scenario.

T1 - the time constant defining the rate of recovery of magnetization (and therefore signal). Brain images with T1-weighted contrast exhibit strong contrast between grey and white matter and are useful for anatomical reference/analysis.

T2 - the time constant defining the loss of magnetization (and therefore signal). Brain images with T2-weighted contrast are often used to identify white matter pathology, typically associated with high water content.

T2* - a measure quantifying MRI signal decay that is enhanced (relative to T2) by microstructural compartments containing tissue constituents, such as iron or myelin, that are susceptible to magnetic fields.

QSM - quantitative susceptibility mapping - a magnetic resonance imaging technique that measures tissue magnetic susceptibility, which has been shown to detect changes in tissue iron, myelin and calcification.

Diffusion tensor - a description of how water diffusion is altered by the presence of tissue membranes. For example, water movement is strongly restricted perpendicular to white matter fibres but weakly along them, resulting in a elliptical diffusion tensor. See also: MD, FA, MO, L1,2,3 [Pierpaoli and Basser, 1996, Smith et al., 2015].

FA fractional anisotropy - a measure of white matter "integrity" derived from a diffusion tensor fit to dMRI data.

MD - mean diffusivity - the average strength of water diffusion, independent of direction.

MO - diffusion tensor mode - a discriminant between (e.g.) the presence of a single strong fibre in a voxel, vs multiple distinct fibres with different directions.

L1,2,3 - in a diffusion tensor fit, the strength of diffusion along the principal axes of the ellipse (eigenvalues).

ICVF intra-cellular volume fraction - an index of white matter neurite density from NODDI modelling of dMRI data (Neurite Orientation Dispersion and Density Imaging [Zhang et al., 2012, Daducci et al., 2015]). Other NODDI modelling outputs include ISOVF (isotropic or free water volume fraction) and OD (orientation dispersion index, a measure of within-voxel tract disorganisation).

CBF - cerebral blood flow - a quantitative measure of the level of perfusion within a region of the brain (units: ml/100g/min)

ATT - arterial transit time - the time taken for blood to travel from the labelling plane to the voxel or region of interest (units: seconds)

B Image processing pipeline - flowcharts

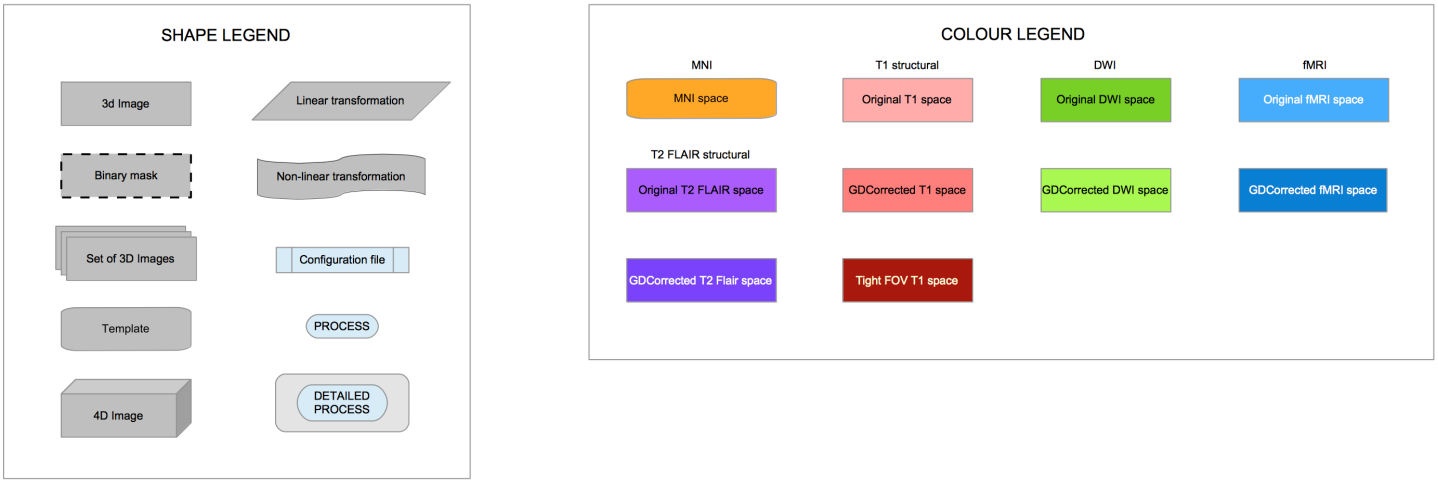

Figure 1: Pipeline flowcharts key.

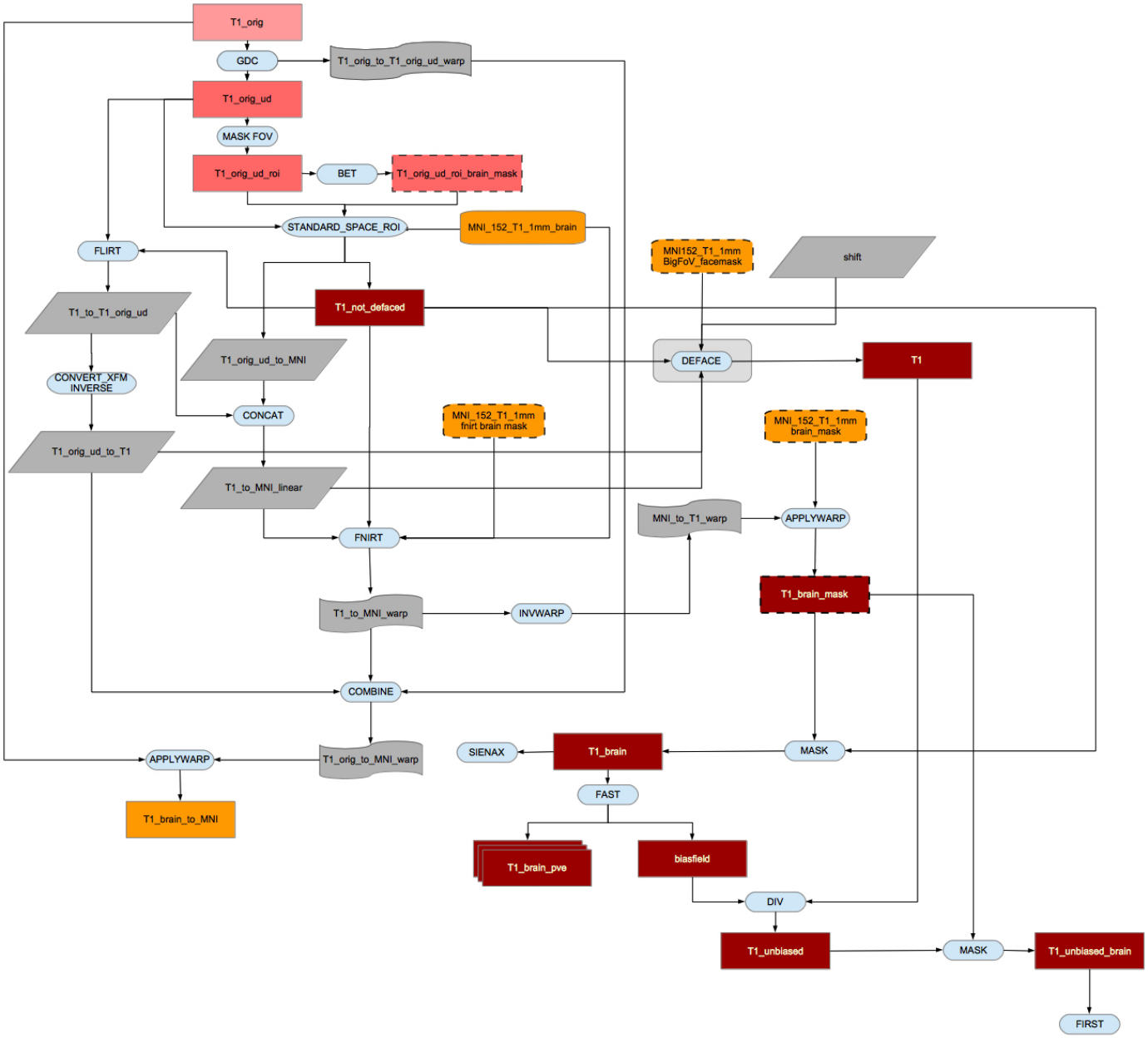

Figure 2: Flowchart for the T1 processing pipeline.

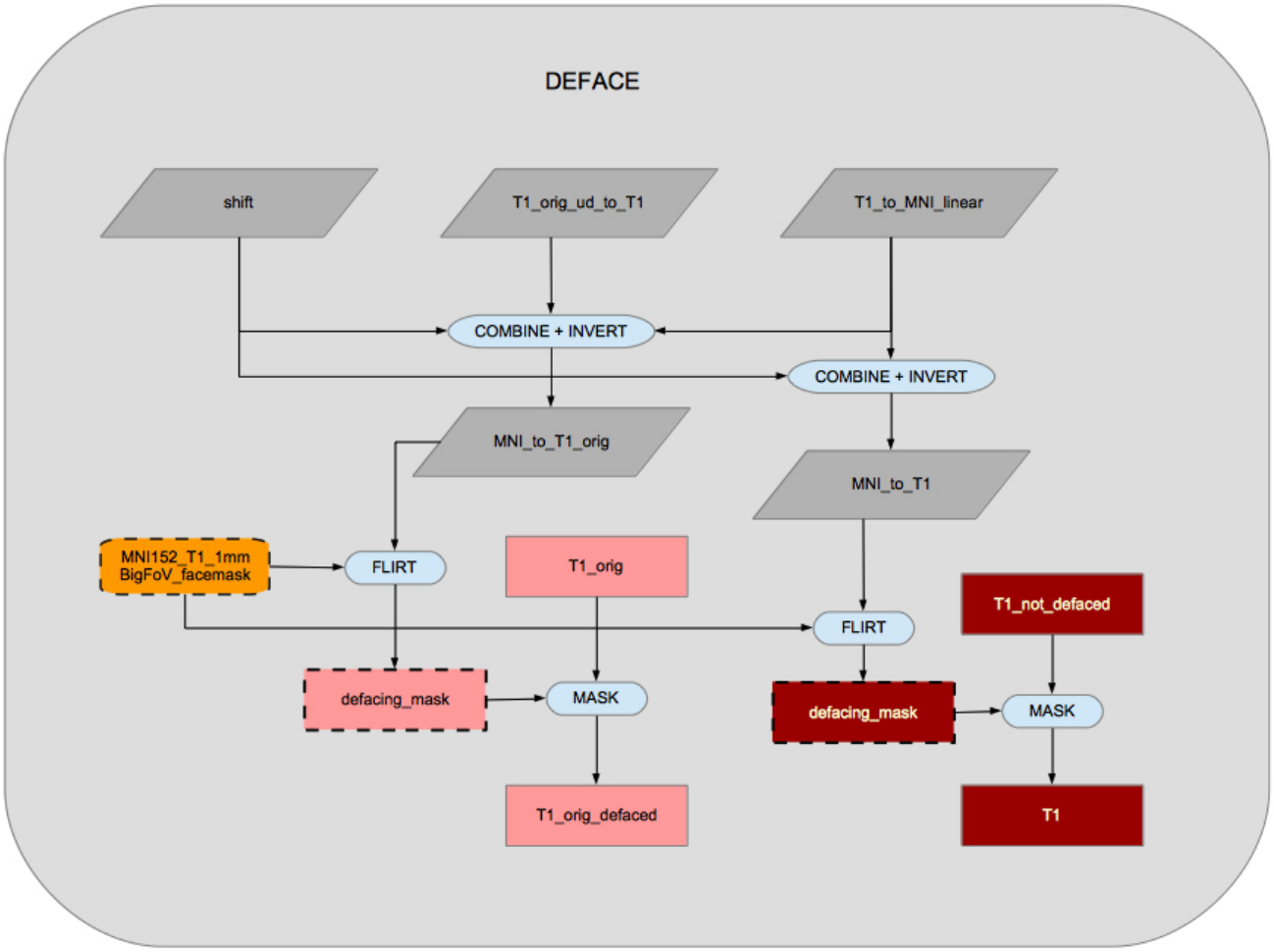

Figure 3: Flowchart for the T1 defacing processing pipeline.

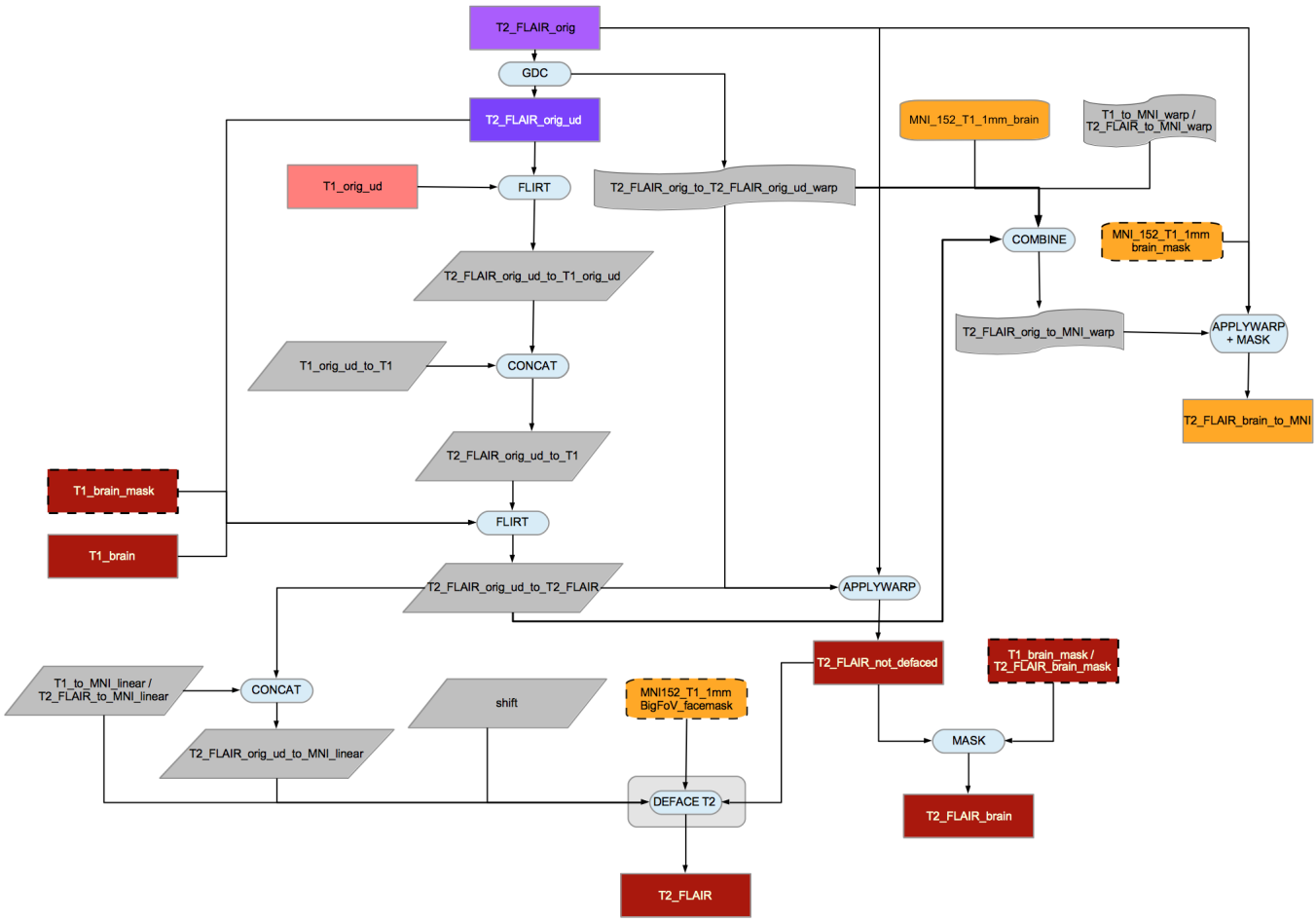

Figure 4: Flowchart for the T2_FLAIR processing pipeline.

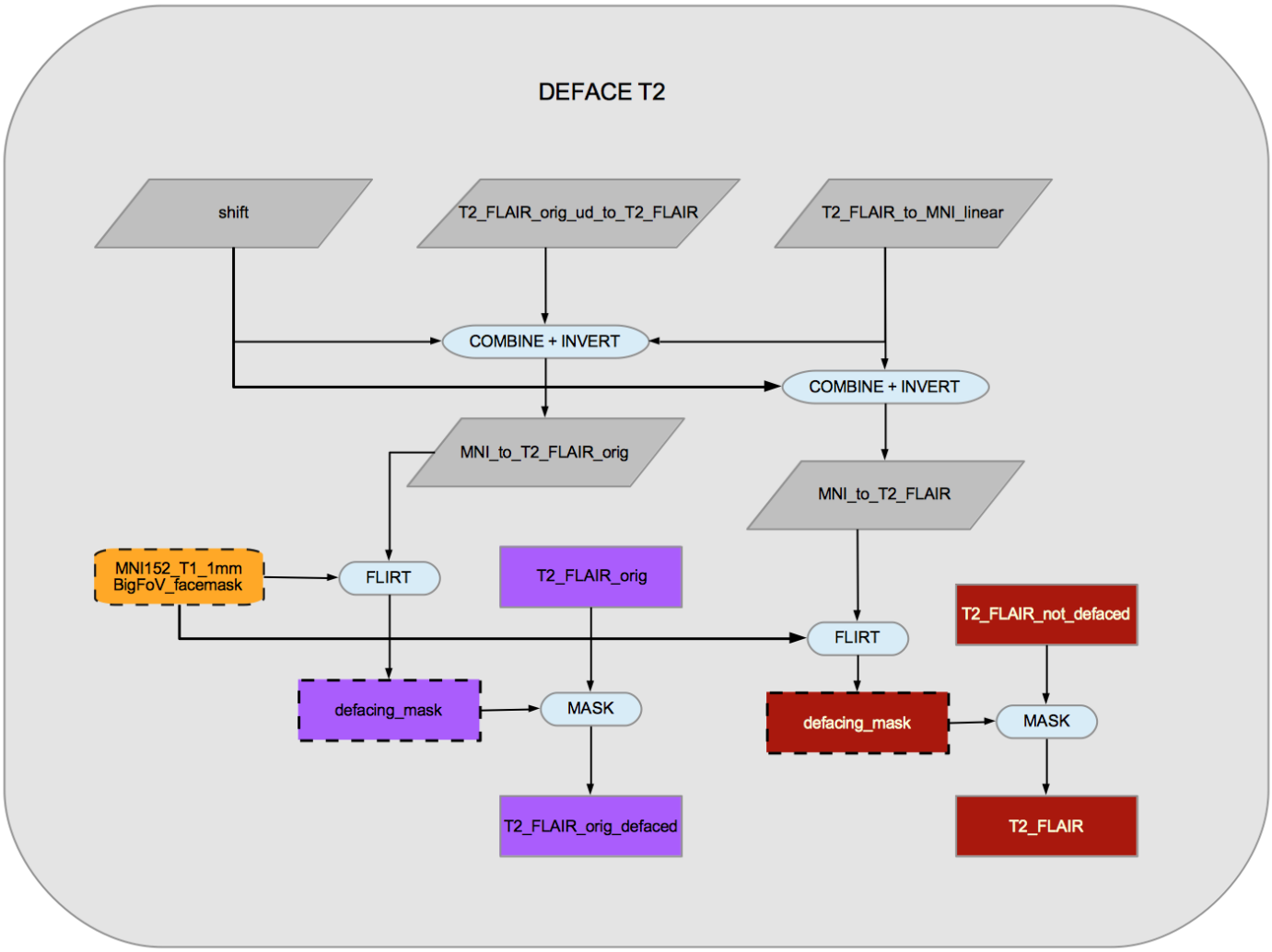

Figure 5: Flowchart for the T2_FLAIR defacing processing pipeline.

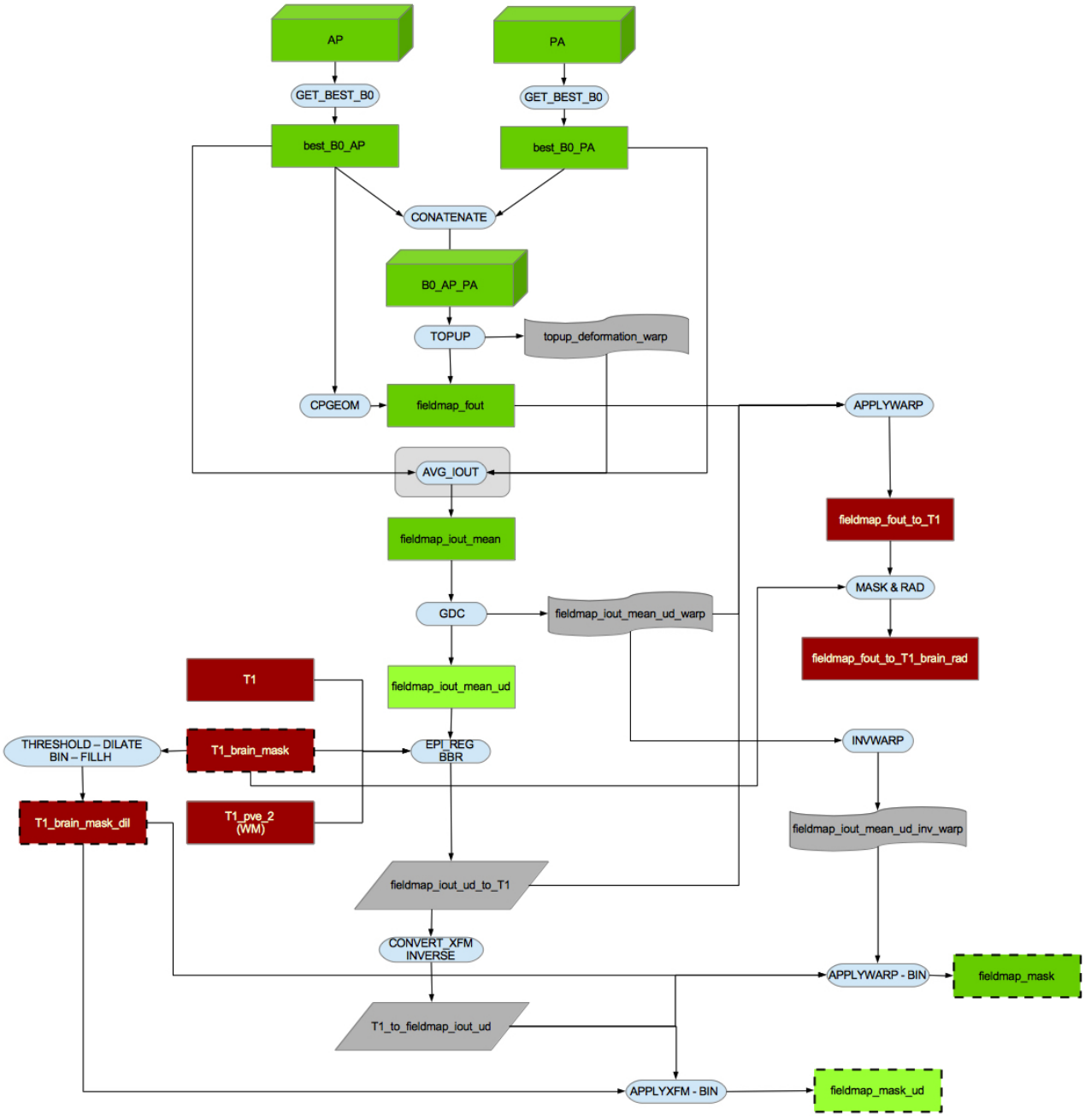

Figure 6: Flowchart for the B0 fieldmap processing pipeline.

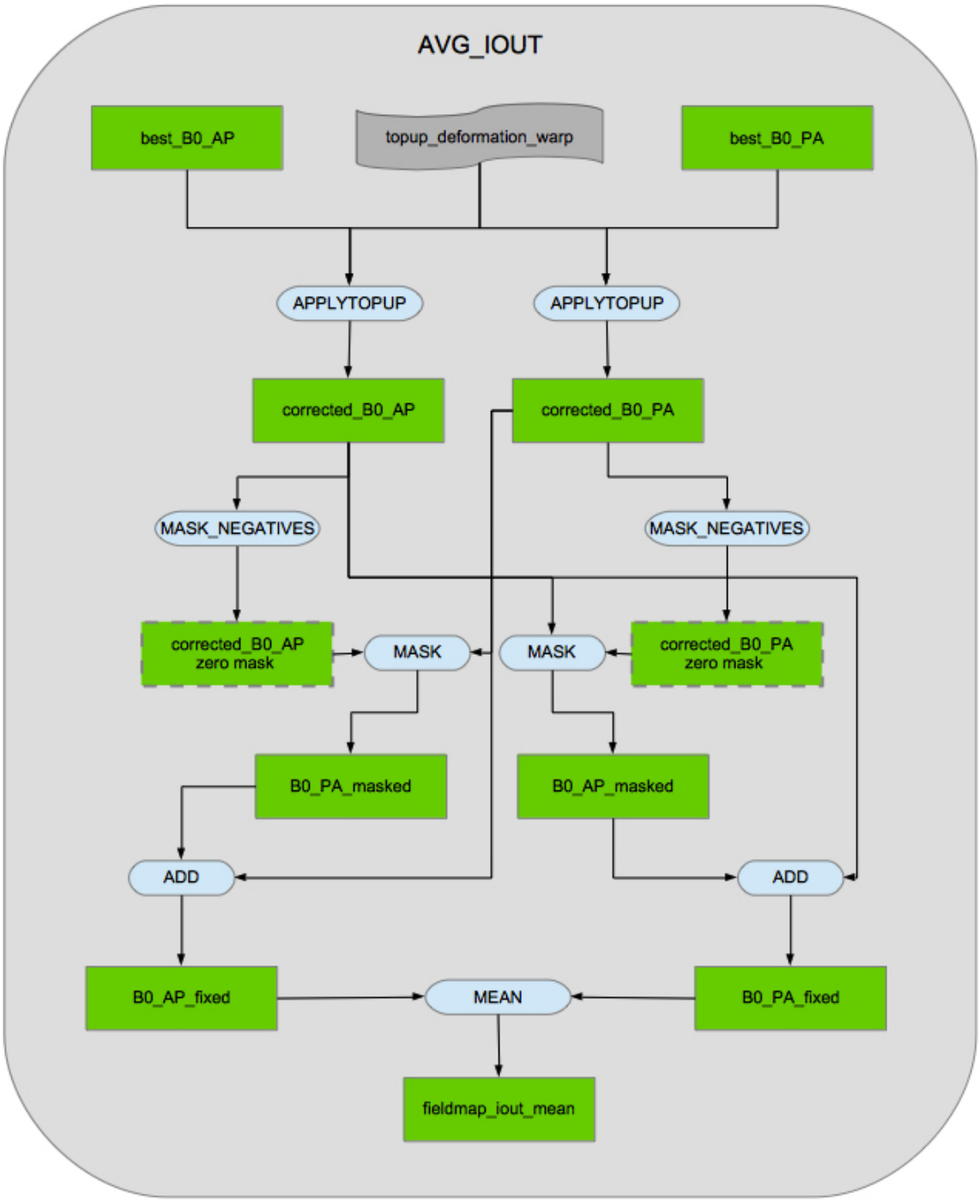

Figure 7: Flowchart for the B0 fieldmap mean magnitude image processing pipeline.

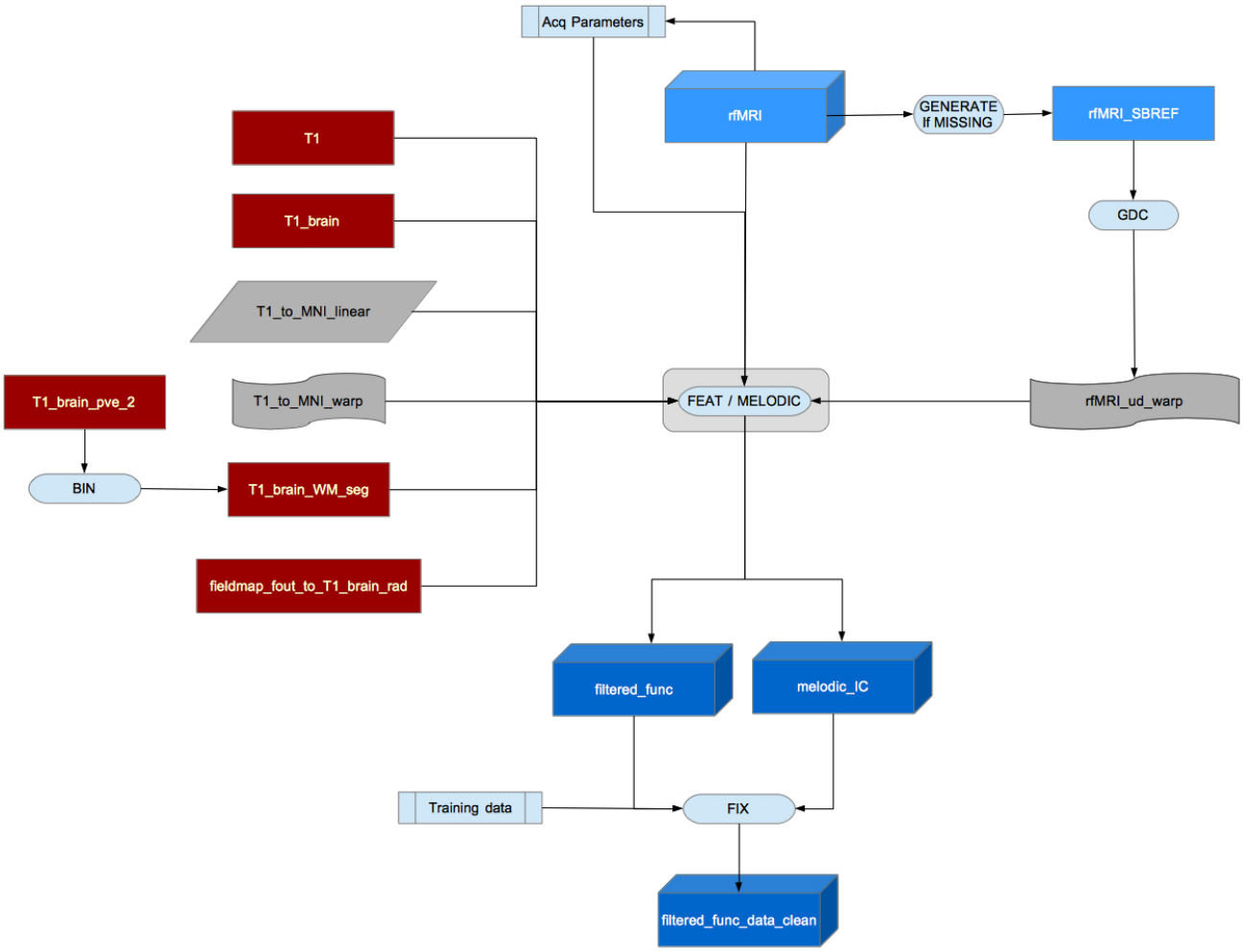

Figure 8: Flowchart for the overall fMRI processing pipelines.

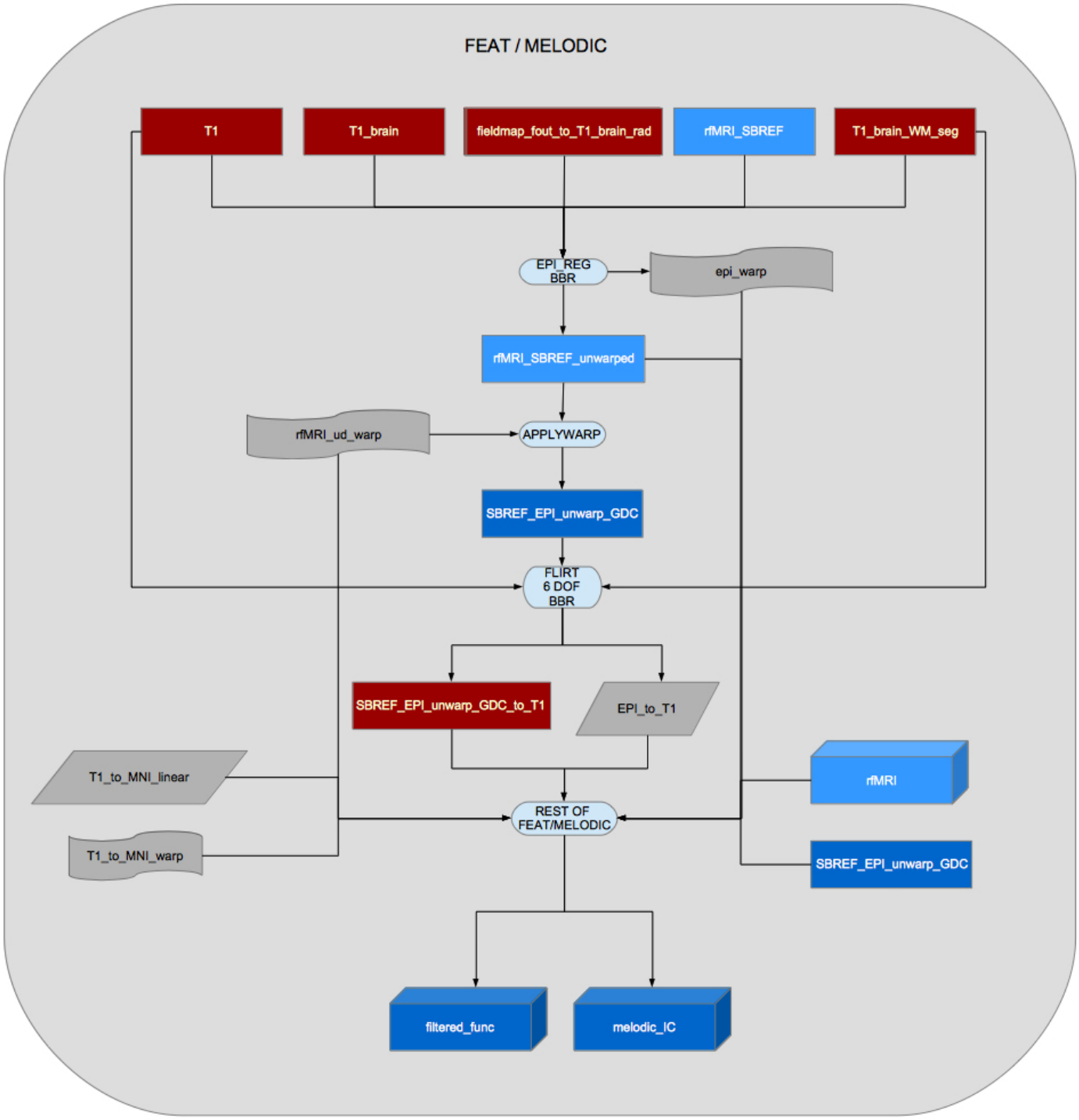

Figure 9: Flowchart for the central parts of the fMRI processing pipelines.

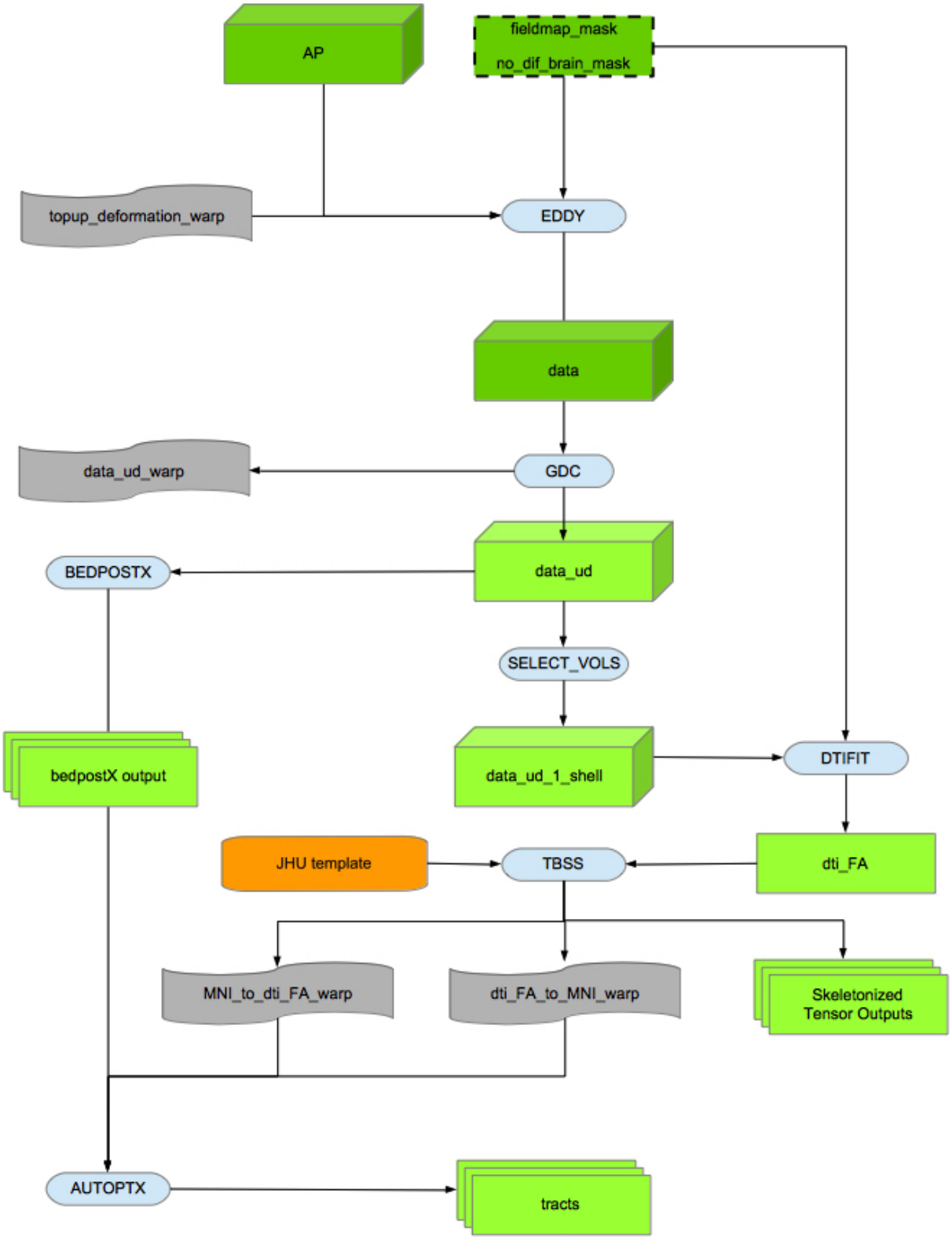

Figure 10: Flowchart for the dMRI processing pipeline.